A New Class of Bragg Stacks and Its Principle Application

Dissertation

zur Erlangung des Grades

„Doktor der Naturwissenschaften“

im Promotionsfach Chemie

am Fachbereich Chemie, Pharmazie und Geowissenschaften

der Johannes Gutenberg-Universität Mainz

Dominik G. Maschke

geb. in Bad Kreuznach

MAINZ, 2010

Die vorliegende Arbeit ist in der Zeit von Februar 2007 bis Juni 2010 im Institut für Anorganische und Analytische Chemie des Fachbereiches Chemie, Pharmazie und Geowissenschaften der Johannes Gutenberg-Universität zu Mainz und im Departement of Chemistry der University of Toronto, Kanada, unter der Betreuung von xxx und xxx entstanden.

Dekan: xxx

1. Berichterstatter: xxx
2. Berichterstatter: xxx

Tag der mündlichen Prüfung: 13.07.2010

Acknowledgement

I would like to thank all the people involved in this work. Without their support this project would not have been possible.

- I am heartily thankful to my two supervisors xxx and xxx. Without their guidance and support this project would not exist. I am specially grateful that they always took time to discuss my projects
- I would like to thank the xxx for financial support
- I would like to acknowledge xxx, for his help and guidance with the ellipsometric characterization
- My gratitude to xxx for the SEM characterization
- My gratitude to xxx for the photoluminescence characterization of the lasing samples. Thanks go to xxx for continuing the project after I left Toronto
- My special thanks to xxx and xxx for the CV measurements and the helpful discussions about this topic
- I would like to thank xxx, xxx and xxx for the excellent cooperation within the phononic crystals project, the BLS characterization and the theoretical calculations
- I would like to acknowledge xxx for the fruitful discussions throughout all the stages of my thesis
- Finally I would like to thank all my lab mates for the good working atmosphere and the fruitful discussions. Special gratitude to xxx for the great time in Toronto

Contents

List of Figures

1. Introduction and Motivation

1.1. Introduction

Color in nature does not exclusively arise from absorption processes. Sea mice, butterflies, and opal gems[1–3] (see Figure 1-1) are examples of so-called "structural color" due to optical

(a) Morpho menelaus[4]. (b) Aphrodita aculeata[5].

Figure 1-1.: Examples of photonic structures, occurring in animate nature.

interference effects from organic or inorganic structures with periodicities in the size-range of visible light. Such constructs are nowadays known as photonic crystals (PC's). At present, photonic crystals are used as non-bleachable dye pigments[6], a new type of display[7, 8], as enhancement for the photo-oxidation[9], or as enhancement for dye-sensitized solar cells[10], to name just a few.

1.2. A Short Introduction into Photonics

A key feature of photonic crystals is periodic variation in the refractive index. This change can happen along one, two or three spatial directions (see Figure 1-2). Therefore, photonic crystals are divided into 1D, 2D and 3D photonic crystals[1].

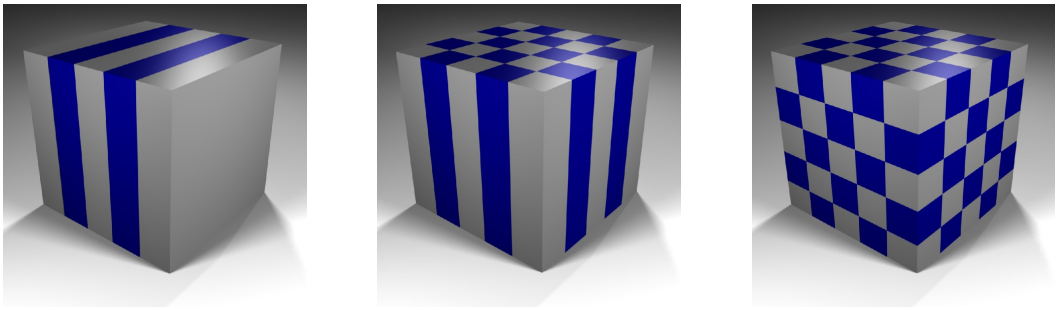

(a) 1D PC. (b) 2D PC (c) 3D PC

Figure 1-2.: Schemes of photonic crystals. The two different colors (blue and white) represent materials with different refractive indices.

3D photonic crystals [3, 11] The most prominent 3D photonic crystal – the opal – is used as a gemstone all over the world. An opal consists of monodisperse, spherical particles, arranged in a fcc lattice (usually produced via self-assembly). The scientific community has put much effort into 3D PC's since they are easy to manufacture and offer an approach to a complete optical band gap[1].

2D photonic crystals [12, 13] These structures are usually produced via lithographic or electrochemical methods. A common 2D PC consists of pillows periodically arranged onto a substrate.

1D photonic crystals [14] They are typically constructed out of layered structures where the refractive index is varied along the stacking direction. In the literature they are also

[1] i.e.: The propagation of light is prevented in all three spatial directions.

known as Bragg stacks, distributed Bragg reflectors (DBR), or Bragg mirrors. Usually two materials with different refractive index are used (e.g. TiO_2 and SiO_2, as high and low refractive index material). Common preparation techniques involve spin-coating, dip-coating or CVD techniques.

1.3. The Photonic Band Structure

The properties of photonic crystals are easy to understand when they are treated as photonic analogs to electronic semiconductors. The periodic variation of the refractive index is comparable to the periodic potential in a semiconductor.

Just like the electronic band structure describes the dependency of the electron energy on its momentum ($E(k)$ vs. k, with k: wavevector), the photonic band structure describes the dependency of the photon energy (h·frequency) on the momentum.

Again, analogous to semiconductors, the photonic band structure may exhibit parts of the energy spectrum that are not allowed, i.e. an optical band gap (see Figure 1-3 on the following page). In the band gap, photons with this energy can neither pass through the photonic crystal, nor can they get absorbed. Thus, they get reflected. Since only a small part of the total spectrum gets reflected, this partial reflection is the source of the structural color.

The photonic properties of Bragg stacks can be estimated using simple mathematical equations[14]. A key feature in the calculation of photonic properties is the optical density $n_x h_x$, where n_x is the refractive index of material x, and h_x is the respective thickness.

The equations needed to calculate certain properties of the spectrum of a Bragg stack can be found in reference[14]. In short, the position of the stop band can be estimated according to:

$$m\lambda_{max} = 2(n_L h_L + n_H h_H) \tag{1.1}$$

where m is the diffraction order, n_L and n_H, h_L and h_H are the refractive indices and the thicknesses of the low and high refractive index material, respectively. This equation shows that a

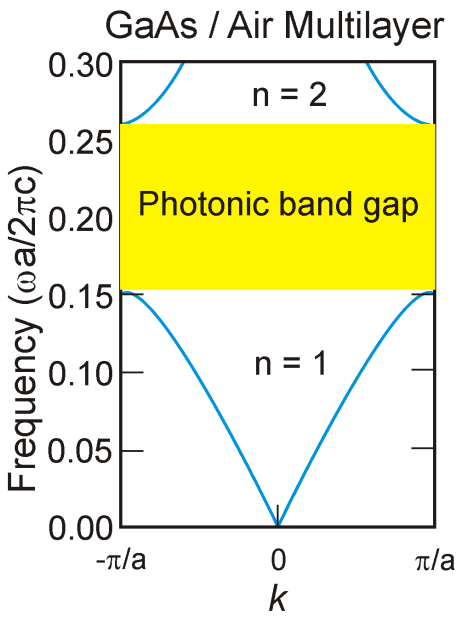

Figure 1-3.: Photonic band structure for on-axis propagation[1]. The layer thickness is 0.5 a and the refractive index is $n_H = 13$ and $n_L = 1$.

thicker layer yields a red-shift of the fundamental reflection. It also shows that there exist higher order reflections at half the wavelength of the fundamental reflection.

The reflectivity can be computed by

$$R = \left[\frac{n_0 - n_s(n_L/n_H)^{2N}}{n_0 + n_s(n_L/n_H)^{2N}}\right]^2 \tag{1.2}$$

where n_0 and n_s are the refractive indices of the surrounding environment and the substrate, respectively, and N is the number of bilayers. This equation demonstrates that the reflectivity (or absorption) gets stronger when the number of bilayers increases.

These equations show that it should be possible to design tailor-made Bragg stacks, and that it should be possible to predict their optical properties with high accuracy.

1.4. State of the Art

Bragg stacks are based on either thin film techniques or mesoscopic assemblies. Thin film Bragg stacks are found in a broad variety of technical applications such as optical interference filters and are produced in large scale at very high optical quality. Despite the broad number of applications, thin films are dense materials that do not offer void volumes to incorporate molecular dyes or reactive species in optical applications like photo oxidation or dye-sensitized solar cells.

The mesoscopic approach[15–17] is intended to overcome this drawback of thin film Bragg stacks. Yet, up to now, there are only a handful of synthesis protocols which are very elaborate for use in either base research or technical application for such a system[2].

1.5. Motivation

A suitable approach to Bragg stacks offering void volumes for molecular dyes or reactive species for use in photo oxidation or dye-sensitized solar cells is to produce them from nanoparticles. Assuming a typical volume demand of a reactive complex of approximately 5 nm and a ccp arrangement of spherical nanoparticles, one may easily derive that the corresponding nanoparticles should exhibit a diameter in the range from 20 to 25 nm (see Section A.1 on page 77). This work will concentrate on the development and characterization of high optical quality Bragg stacks. They are made from SiO_2 and TiO_2 nanoparticles in such a way that they are suitable for use as hosts for reactive species or dye molecules. This work will also demonstrate the proof of principle for their use in optical applications that rely on reactive species inside the void volumes.

[2] The usual aging time for a meosporous Bragg stack is 18 h - 2 days per layer[15].

2. Coating of Bragg Stacks

2.1. Introduction

2.1.1. Stable Nanoparticle Solutions

To produce Bragg stacks with high precision, high quality and with a uniform coating of the substrate, it is necessary to have high quality coating solutions. Nanoparticles that are well suited for spin-coating should exhibit only a very low tendency towards agglomeration. Agglomerated particles scatter light resulting in a turbid solution, which makes them easy to recognize. If the size of the used nanoparticles (usually 15 - 25 nm) is well below the wavelength of light, the particles exhibit no scattering of light in the visible spectrum and the solution appears clear. However, if larger agglomerates exist, light scattering at these aggregates leads to a white color. Such agglomerates would destroy the photonic effect by bouncing the light in many directions instead of only acting as active medium. They would prohibit the coating of thin smooth layers but lead to bumps in the surface. This would not lead to a photonic structure with a band gap.

Consequently, the size of the particles should be at around 20 - 25 nm. This makes it possible to coat layers, thin enough for a fundamental reflex in the UV-region and it also exhibits a pore size large enough to infiltrate bigger molecules.

Solutions of silica nanoparticles are commercially available as LUDOX®AS-30-solutions supplied by Aldrich®. Solutions of titania-nanoparticles fulfilling the criteria above could nei-

ther be found by a commercial supplier nor in the scientific literature. In most cases a state of the art synthesis of TiO_2 nanoparticles requires the following steps according to two prominent procedures from Burnside et al.[18] and from Barbé et al.[19]: The TiO_2 is first precipitated by pouring Titanium(IV)isopropoxide in an aqueous solution, yielding crude water-rich TiO_2 which exhibits large agglomerates. In the next step the TiO_2 is peptized, which means that the large agglomerates are dispersed into small individual particles. The peptized particles are well suited for simple Bragg stacks since they have almost no tendency to form agglomerates. However, the particles remain still very small (around 7 nm) which limits their use for infiltration of larger molecules. In the next step these particles undergo hydrothermal growth, increasing their size to 20 nm large particles. These large nanoparticles show a strong tendency to form large agglomerates. Long-time sonication (10 min) with a sonicator horn was tried out to brake those agglomerates but did not yield an improvement. Hence, they are not suited for the coating of Bragg stacks.

Therefore, a new synthesis for TiO_2 nanoparticles in solution was developed that leads to well-dispersed particles with a diameter of 25 nm, forming a clear solution without traces of agglomerates and therefore needs no filtration. To achieve the two controversy goals of this synthesis, namely large particles and no agglomeration, a ligand had to be used. The ligand should feature the following properties to be suited for this synthesis:

Strong attachment to TiO_2 To functionalize the TiO_2 particles, the ligand needs strong adhesion to the TiO_2 surface. It has to withstand the 200 °C conditions of the hydrothermal growth step and pH changes should not dissolve the ligand from the surface. Catechol-type ligands are ideally suited for these tasks.

Small size Each ligand molecule should only bind to one TiO_2 particle. Bridging of two or more particles by one ligand would lead to the formation of agglomerates.

Electrostatic repulsion In analogy to milk, where charged proteins on the surface of the

fat droplets provide an electrostatic repulsion strong enough to prevent agglomeration, the ligand of choice also needs a strong electrostatic repulsion. This repulsion can be provided by a charged functional group. Since the particles were synthesized in alkaline solution, a carboxy-group is well suited for this.

Combining the above mentioned criteria, one ends up with a catechol, to which a carboxy-group is closely attached. The 3,4-dihydroxyhydrocinnamic acid (DHCA, see Figure 2-1) combines all of these criteria. The catechol has a strong attachment to the TiO_2 and binds under

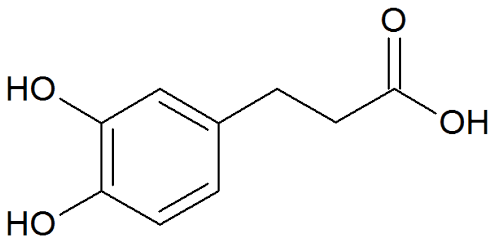

Figure 2-1.: 3,4-Dihydroxyhydrocinnamic acid.

alkaline conditions while the carboxy-group produces a negative electrostatic repulsion which yields a good separation of the individual particles. In addition, the catechol-group works as an indicator for functionalized TiO_2 particles because it forms a deep-red colored complex when it is attached to TiO_2. The function principle of the ligand is shown in Figure 2-2 on the next page.

2.1.2. Uniform Coating of Substrates

With the optimized synthesis of TiO_2 nanoparticles (see Section 2.3.1 on page 32) and the available SiO_2 nanoparticles, it is now possible to optimize the coating conditions in order to obtain a uniform coating of the substrate. Only with a uniform thickness throughout the whole substrate, which is usually 2 x 2 cm, it is possible to obtain Bragg stacks that exhibit a uniform color and a high reflectance throughout the substrate. "Comets" and "striations" are among the common defects encountered in spin-coating. Striations are radially oriented variations of the

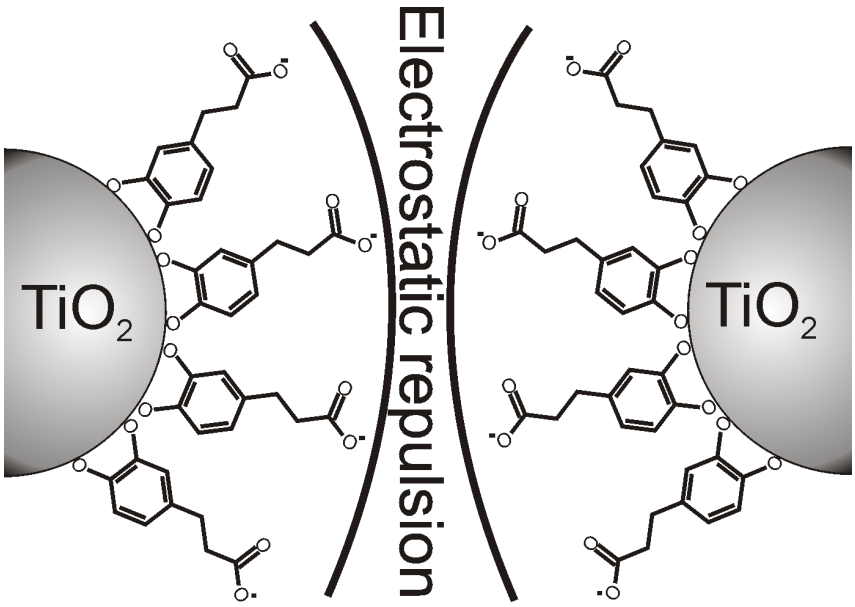

Figure 2-2.: Function principle of the DHCA-ligand ontop of TiO_2 nanoparticles.

the film thickness and a result of the rotation of the surface cell pattern. Comets are point defects in the film uniformity, caused by large agglomerates such as agglomerated nanoparticles or dust. These agglomerates can be present in the spin-coating solution or form upon coating[20].

The following spin-coating parameters have great influence on the uniformity of the coating:

Speed A high speed yields high shear forces on the liquid which are much stronger than the surface tension of the liquid. This leads to a more uniform coating at the borders of the substrate.

Acceleration A fast acceleration ensures fast evaporation of the solvent and, therefore, a fast increase of liquid-viscosity. This prevents particle agglomeration and, consequently, the formation of comets[20].

Time The time has to be chosen to be sufficient for complete evaporation of the liquid. After this step, there is no decrease in film thickness. A shorter time however, leads to an inhomogeneous coating.

Additives Additives in the coating solution can be used to drastically improve the homogeneity of the coating. They have a great influence on the surface-tension, which is important for a uniform coating

The initial optimization of the process parameters was performed using Si-wafers. They offer a better image quality in SEM investigations, but most importantly, unlike glass, on which the films are barely visible with the naked eye, the films on Si-wafers exhibit a strong coloration, resulting from interference effects. This coloration makes it possible to locate variations in the film thickness by observing variations in the film color. Therefore, a uniform color equals a uniform thickness. Additionally, the surface of a Si-wafer consists of SiO_2 and, therefore, is very similar to the surface of a glass substrate.

2.2. Results and Discussion

2.2.1. Effect of the DHCA-Ligand on Titania Nanoparticles

The synthesis of the DHCA-functionalized TiO_2 particles was performed according to a modified synthesis of Burnside et al.[18]. The schematic of the synthesis is shown in Figure 2-3 on the next page, details about the synthesis can be found in the experimental part in Section 2.3.1 on page 32.

To demonstrate the effect of DHCA-concentration onto the solubility and agglomeration behavior of the TiO_2 nanoparticles, the particles were synthesized according to the procedure in Section 2.3.1, varying only the concentration of the DHCA-ligand and keeping the other parameters constant. Some approximations about the amount of DHCA ligand needed for the experiments are discussed in the Appendix in Section A.2 on page 78. The resulting solutions are shown in Figure 2-4 on page 13. On the left-hand side of the picture, the solution is cloudy and white, large agglomerated particles scatter the light. By increasing the DHCA concentration, the intensity of the red color increases which is due to an increased amount of catechol,

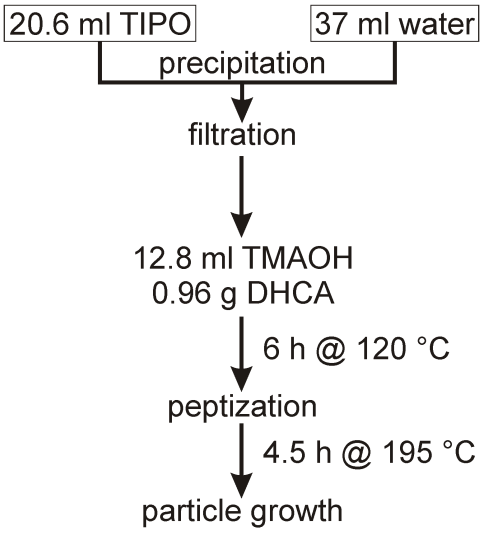

Figure 2-3.: Schematic of the synthesis for the DHCA-functionalized TiO_2 nanoparticles. TIPO: Titanium(IV) isopropoxide, TMAOH: Tetramethylammonium hydroxide and DHCA: 3,4-Dihydroxyhydrocinnamic acid.

attached to the TiO_2 surface. But also the cloudy nature of the solutions vanishes, due to the electrostatic repulsion of the ligands which keeps the particles apart. This yields into a transparent solution of individual nanoparticles in an alkaline, aqueous solution that is perfectly suited for the production of Bragg stacks.

To analyze the influence of the DHCA-ligand onto the shape of the particles, SEM images were taken from each solution shown in Figure 2-4. The SEM images are shown in Figure 2-5 on page 14.

In image 2-5(a), where no DHCA is used, large bipyramidal particles dominate the image. The particles exhibit a slight anisotropy. In Figure 2-5(b), where 0.08 % DHCA is used, there are still mostly large particles and the overall impression resembles the previous image. When the amount of DHCA is increased to 2.22 % and 2.86 %, the amount of large particles on the surface of the film decreases drastically. However, there are still some large particles on the bottom of the film which only appear when the film is scratched.

By further increasing the DHCA concentration, the effect gets even more pronounced until

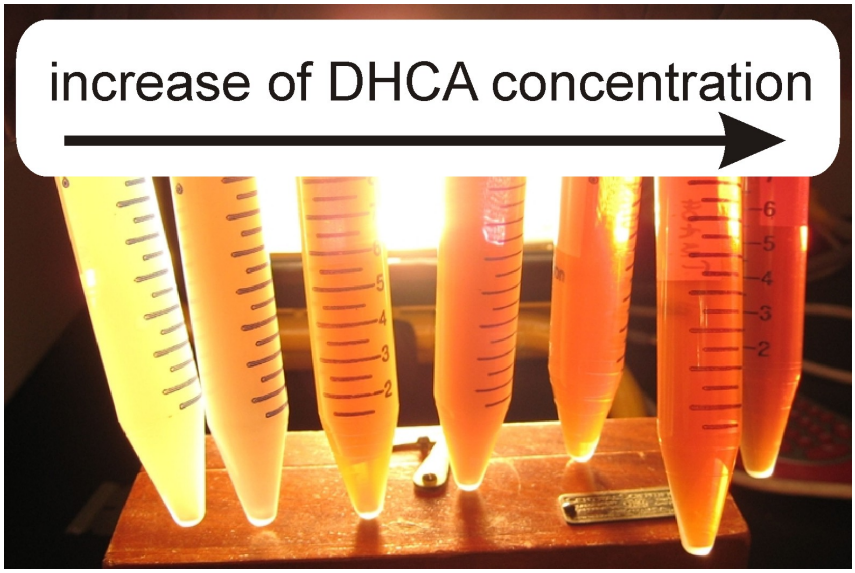

Figure 2-4.: Titania-nanoparticles with increasing amount of DHCA. DHCA concentration (DHCA/TiO_2, w/w) from left to right: 0 %, 0.08 %, 2.22 %, 2.85 %, 4.28 %, 5.63 % and 7.62 %.

7.62 % of DHCA are added to the reaction mixture (see Figure 2-6 on page 15). The particles are mostly spherically shaped, only a small number resembles the bipyramidal shape from the solutions with a low concentration of DHCA. The sample looks much more homogeneous. They also form a very homogeneous coating on the substrate, which is depicted in figure Figure 2-6(b) on page 15.

The size distribution was analyzed using DLS (see Figure 2-7 on page 15). The DLS-data shows an unimodal dispersion of the particle sizes, centered at 25 nm. This is in very good agreement with the observation from the SEM images.

2.2.2. Spin-Coating of Bragg Stacks

Optimization of the spin-coating procedure was done on Si-wafers. The wafers were cleaned using a piranha solution as described in Section 2.3.2 on page 32. To investigate the influence

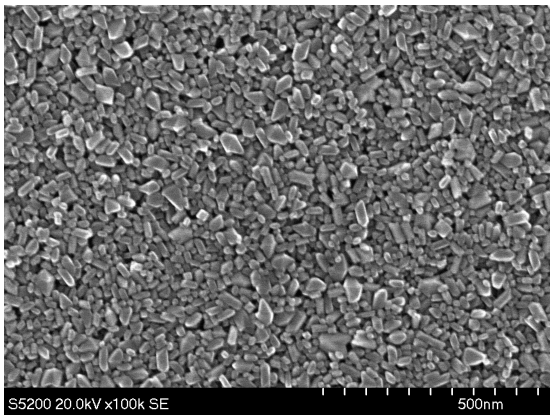

(a) 0 % DHCA

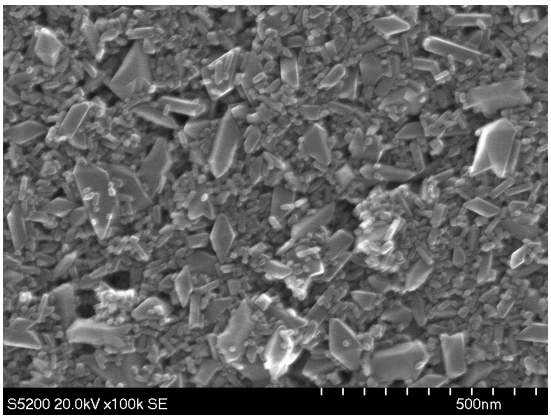

(b) 0.08 % DHCA

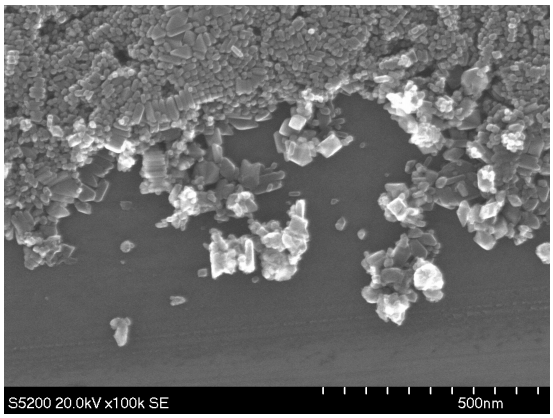

(c) 2.22 % DHCA

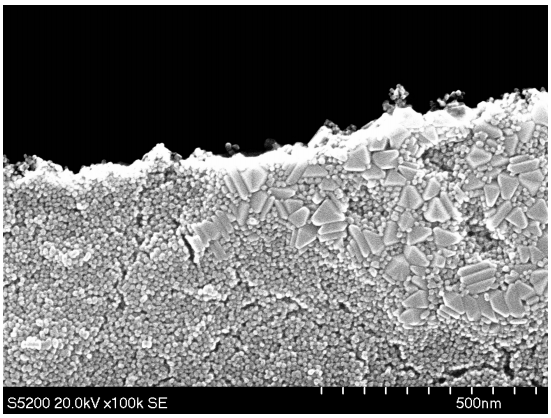

(d) 2.85 % DHCA

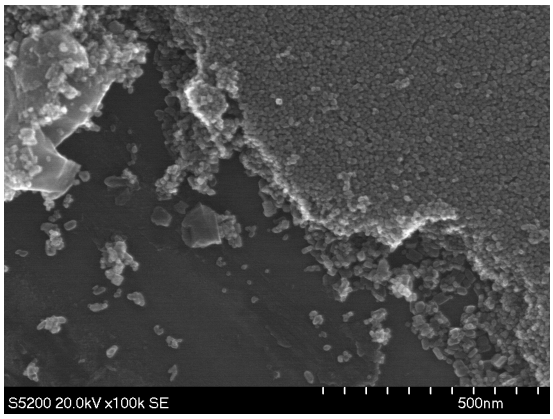

(e) 4.28 % DHCA

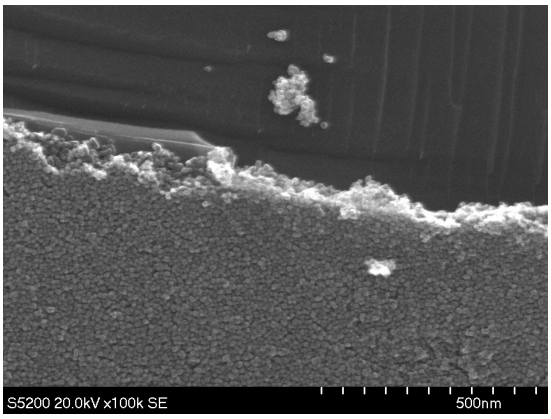

(f) 5.63 % DHCA

Figure 2-5.: SEM images, showing the effect of increasing DHCA concentration.

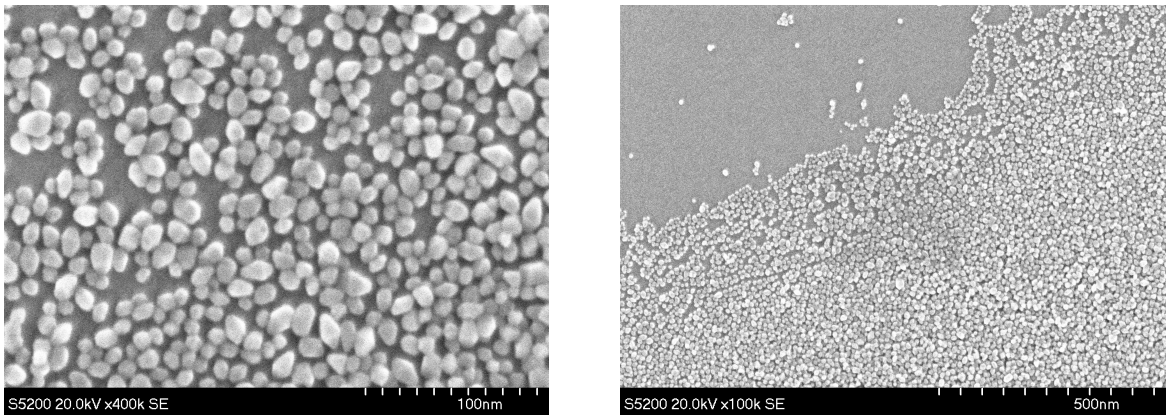

(a) (b)

Figure 2-6.: SEM images, showing the titania particles with 7.62 % of DHCA (w/w). These were the type of particles used for the rest of this work.

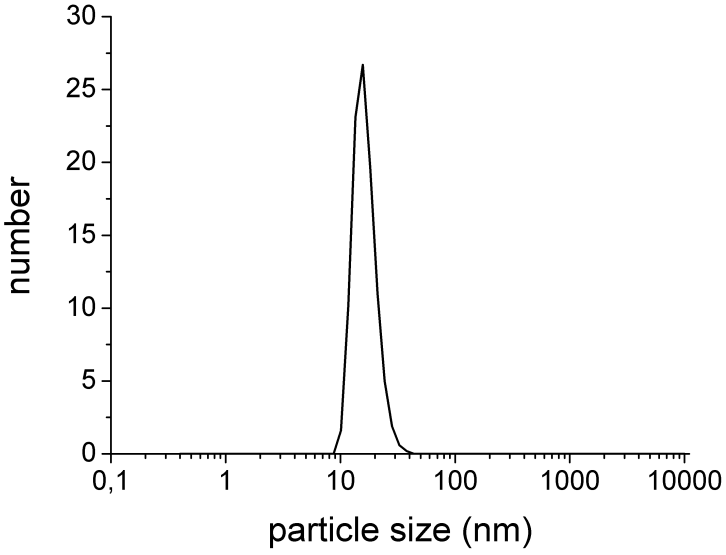

Figure 2-7.: Particle numbers vs. particle size, obtained by DLS.

of the rotation frequency[1] on the film quality, the crude solution of the TiO_2 nanoparticles obtained from the synthesis described in Section 2.3.1 on page 32 was spin-coated, varying only the coating speed. The result is shown in Figure 2-8.

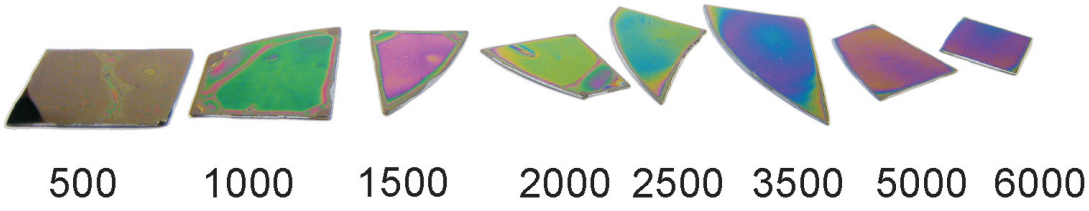

Figure 2-8.: Coating of crude titania solution on Si-wafers. No additives were added and the coating speed was varied.

The sample with 500 rpm shows only some coloration at the very center of the sample. When the speed is increased, the samples exhibit a prominent coloration, however, the color is not uniformly distributed on the substrate. Point defects and many different colors dominate the impression of the substrate. At 3500 rpm and higher, the color gets more uniform, there are less defects, but there is still no completely uniform color throughout the sample. Although none of the samples has a uniform color throughout the hole substrate, it is obvious that an increased spin-coating speed leads to a better film quality.

The problems that were present in the previous examples (see Figure 2-8) are attributed to the high surface tension of the solution. This prevents the solution to uniformly wetten the surface, leading to an inhomogeneous coating with TiO_2 nanoparticles. One way to decrease the surface tension in a solution is to add an amphiphile. Since the used nanoparticles are stabilized under alkaline conditions, an amphiphile which is stable under alkaline conditions was added. In this case sodium dodecyl sulfate (SDS) (stored as 10 % solution in ammonium hydroxide solution) was used. The previous experiment was repeated adding 500 ppm SDS to the crude TiO_2 solution. The result is shown in Figure 2-9 on the next page.

[1] Furthermore, this is referred to as speed.

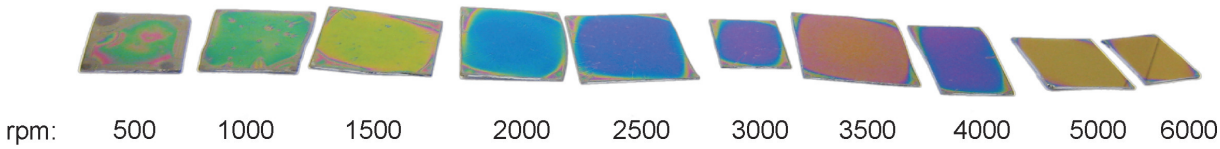

Figure 2-9.: Titania-solution spin-coated on Si-wafers with 500 ppm SDS added for a more homogeneous coating.

The image shows an inhomogeneous coating for the speed of 500 and 1000 rpm but at higher speed the coating gets more homogeneous until at 5000 rpm a very uniform coating is achieved with only small variations in the color at the edges of the sample. This color-variation at the edge of the substrate is attributed to the Marangoni-effect[21, 22], which is an intrinsic defect in spin-coating and cannot be circumvented. Nevertheless, this effect is localized only at the very edge of the substrate. The majority shows a uniform color and thickness. At 6000 rpm the shear forces on the sample were too large so that some samples did not stay attached to the spin-coater throughout the whole process. 5000 rpm were chosen to be the best compromise in terms of high quality and uniformity and yield.

With the best suited spin-coating speed determined to be at 5000 rpm, the influence of SDS on the quality and thickness of the TiO_2 films had to be investigated. Therefore, different amounts of SDS were added to the crude TiO_2 solutions. Spin-coating parameters are shown in Table 2.1. The resulting Si-wafers are shown in Figure 2-10 on the next page. While the

Table 2.1.: Spin-coating parameters.

Speed	5000 rpm
Acceleration	5040 rpm/s
Time	20 s

samples on the left-hand side with SDS concentrations of 200 and 500 ppm still have a large

degree of inhomogeneous coating, on the other hand, the samples with 700, 1000 and 1200 ppm SDS show a very uniform coating. The samples from 1500 - 3000 ppm SDS however show a high degree of comets, which is attributed to bubbles that form upon the spin-coating process. For the rest of this work 1000 ppm of SDS was added to all aqueous spin-coating solutions.

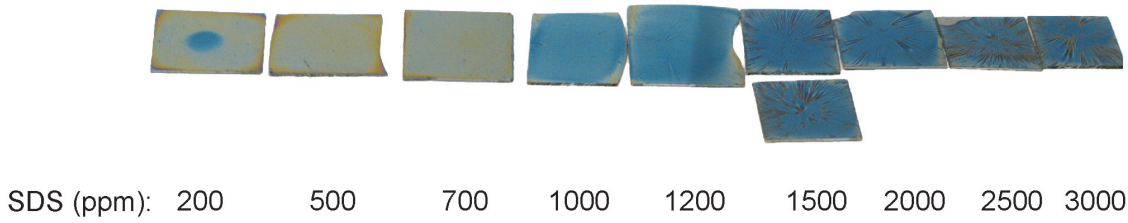

Figure 2-10.: Optical image of Si-wafer coated with TiO_2 nanoparticles. Speed, acceleration and time was kept constant, SDS concentration was increased from left-to-right.

In order to determine the dependency of the film thickness on the SDS concentration and on the spin-coating speed, two sets of experiments were conducted. In the first set the speed of the spin-coater was kept constant and the concentration of SDS was varied. The samples were then examined using cross-section SEM and the thickness was determined. The result is shown in Figure 2-11 on the facing page. The average thickness is at 130 nm and the SDS has very little effect on the film thickness.

To determine the effect of the coating speed onto the film thickness, 1000 ppm SDS were added to a solution, and this solution was spin-coated at different speeds. These samples were again analyzed taking cross-section SEM images. The result is shown in Figure 2-12 on the next page. The film thickness shows only little variation upon variation of the coating speed, averaging the film thicknesses at approximately 120 nm[2].

Since the spin-coating of SiO_2 nanoparticles proved to yield good quality with the conditions used for the TiO_2 nanoparticles (1000 ppm SDS, spin-coater settings, speed 5000 rpm,

[2]Please note that the here used TiO_2 solution was more dilute than the previous one.

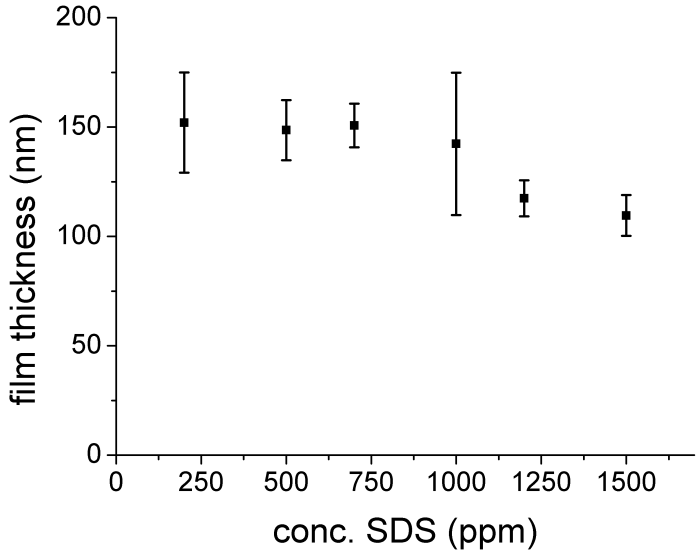

Figure 2-11.: Plot of film thickness vs. SDS concentration. Coating parameters: speed 500 rpm, acceleration: 5040 rpm/s and time: 20 s.

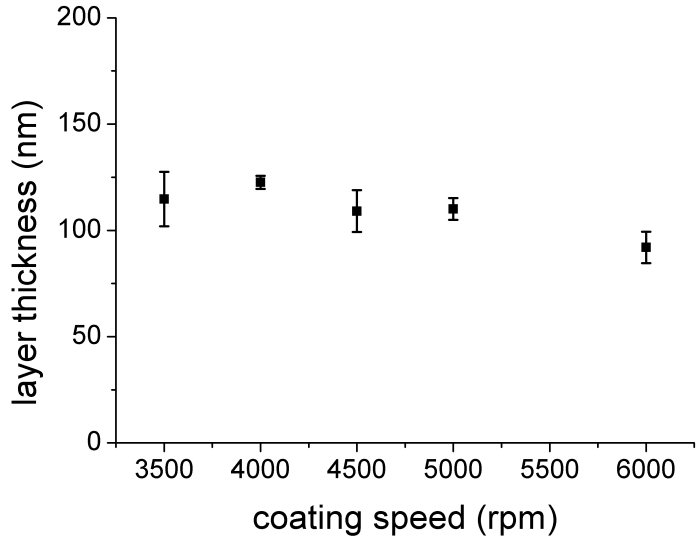

Figure 2-12.: Plot of film thickness vs. coating speed. Spin-coating parameters: speed: varied, acceleration: 5040 rpm/s and time: 20 s.

acceleration: 5040 rpm/s, time: 20 s), the same settings were used for spin-coating of SiO_2 nanoparticles.

Since the film thickness is invariant for neither the amount of SDS nor the speed of spin-coating, this leaves only one parameter remaining in order to control the film thickness. Namely the concentration of the coating solution. Its influence on the film thickness is shown in the next section (Section 2.2.3).

2.2.3. Thickness Calibration of Nanoparticle Solutions

Multiple experiments with a spectroscopic ellipsometer provided information about how the concentrations of the spin-coating solutions influence the layer thickness, the void space, and the non-uniformity. With an spectroscopic ellipsometer it is possible to obtain the following data:

Thickness The thickness of the measured film. It is also possible to obtain the thickness for a multi layered structure consisting of two materials. These data are a very important tool to predict the actual position of the stop band.

Void space The space in a film that is not occupied by the primary material, in this case SiO_2 or TiO_2. The void space is given in vol.-% of air.

Film non-uniformity The homogeneity of the film at the measured spot. The lower the number, the more homogeneous the film is.

Since spectroscopic ellipsometry measures a much larger spot than for example cross-section SEM investigation, the ellipsometric data are more representative for the films than those from SEM investigations. Two identical samples were spin-coated and analyzed.

The composition of the spin-coating solutions that were used are described in section 2.3.3 on page 33 in Table 2.2 and 2.3. All experiments were conducted on Si-wafers cleaned in a piranha solution as described in Section 2.3.4 on page 34. To get rid of adsorbed water inside the pores,

the samples were subjected to heat treatment at 450 °C prior to the actual measurement.

The ellipsometric experiments were conducted using a variable angle spectroscopic ellipsometer (VASE, J. A. Woollam, Lincoln, NE). In the angular range of 70° to 75° in steps of 5° with a spectral range from 200 - 1700 nm in steps of 10 nm. The resultant graphs were fitted using the software provided by the manufacturer to yield the desired data.

Ellipsometric Calibration of the Single Layer Thicknesses

The first set of experiments gave information about the thickness, void space, and non-uniformity of a single layer of either SiO_2 or TiO_2 on a Si-wafer. This information is important as reference to the multilayer setups. Therefore, piranha-cleaned Si-wafers were coated with a single layer of SiO_2 or TiO_2 of different concentrations. This set of experiments is further referred to as *thickcal*. A sketch of the sample setup is shown in 2-13(a) on the next page.

The results from the ellipsometric characterization are shown in Figure 2-13 on the following page. All samples show a non-uniformity between 0 % and 20 % and the void space varies only slightly around 34 %. The film thickness increases linearly with the concentration of the coating solutions. The increase in thickness per g/l was fitted using a linear regression through the origin. The slope is: 1.46 and 0.90 nm/(g/l) for SiO_2 and TiO_2, respectively. No hint of a substrate effect was observed.

Ellipsometric Calibration of the Multi-Layer Thicknesses

The next set of experiments gave insight into the influence of the substrate and the influence of the previous layer on the subsequent layer. Therefore, piranha-cleaned Si-wafers were coated with multiple layers of TiO_2 and SiO_2 nanoparticles with concentrations of 180.4 g/l and 70 g/l, respectively. Between each coating cycle the samples were subjected to heat treatment for 1 h

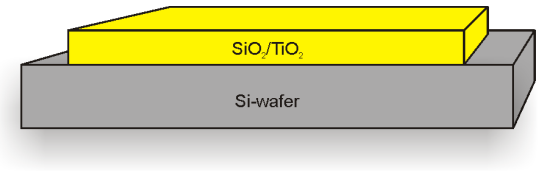

(a) Sketch of the sample setup.

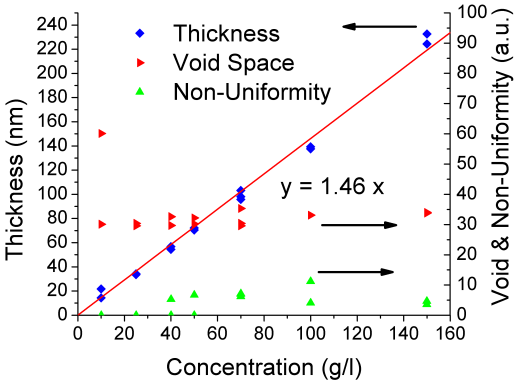

(b) Ellipsometric data for thickcal-silica.

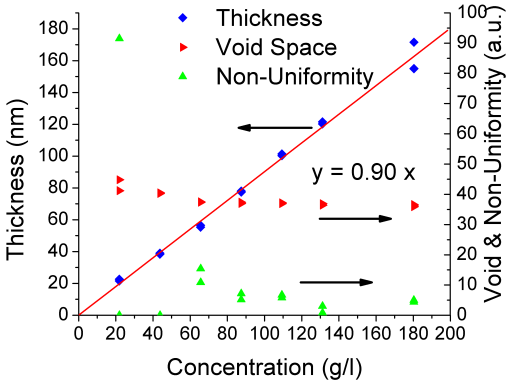

(c) Ellipsometric data for thickcal-titania.

Figure 2-13.: Sketch of the setup for the thickcal samples and the results from the ellipsometric characterization. The linear regression yields an $R^2 = 0.998$ and $R^2 = 0.999$ for SiO_2 and TiO_2, respectively.

at 450 °C. In the graphs the thickness of layer 1, 2, 3 and 4 is plotted against the number of layers. The void space and the non-uniformity was also examined. This set of experiments is referred to as *multistack*. A sketch of a sample setup is shown in Figure 2-14(a).

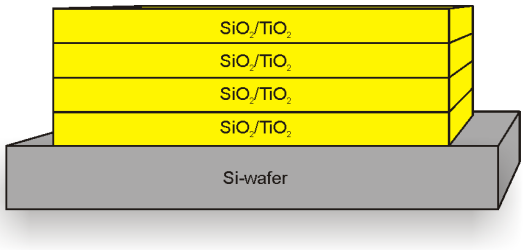

(a) Sketch of the sample setup.

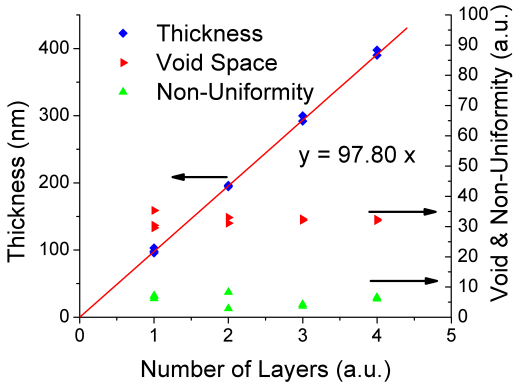

(b) Ellipsometric data for multistack-silica.

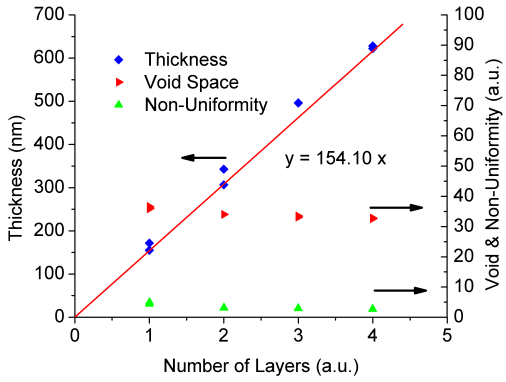

(c) Ellipsometric data for multistack-titania.

Figure 2-14.: Sketch of the setup for the multistack samples and the results from the ellipsometric characterization. The linear regression yields an $R^2 = 0.9998$ and $R^2 = 0.9995$ for SiO_2 and TiO_2, respectively.

The void space and the non-uniformity matches those values observed on a single layer in the *thickcal* set of experiments. The thickness increase in 2-14(b) for the stack with SiO_2 layers is 97.8 nm/layer as has been found out by linear regression through the origin. For comparison, in the thickcal set of experiments a SiO_2 solution with a concentration of 70 g/l had a thickness of 99.4 nm in average. There is no substrate effect observed when SiO_2 is coated on a Si-wafer.

The thickness increase for the titania multistack experiments is 154.1 nm/layer. This matches the thickness of the previous experiment (see Figure 2-14(c) on the preceding page), where a single layer of TiO_2 nanoparticles coated from a solution with 180.4 g/l had a thickness of 160.5 nm in average. Neither can a substrate-effect be observed.

Ellipsometric Calibration of the Multi-Layer Thicknesses in a SiO_2/TiO_2 Stack

In the last set of the ellipsometric investigations, the influence of a SiO_2 layer on a TiO_2 layer and vice versa was examined. Therefore, multilayer-stacks consisting of SiO_2 and TiO_2 layers, always starting with TiO_2 on the substrate, were produced. Each stack consisted of three bilayers (six layers in total). In one set of experiments every layer with an odd number (1, 3 and 5) was made out of TiO_2 from a solution with a concentration of 180.4 g/l. The even layers (2, 4 and 6) were made out of SiO_2 and the concentration of the spin-coating solution was varied from 10 - 150 g/l (see Table 2.3 on page 34). At each individual sample the concentration of the SiO_2 solution was kept constant. A sketch of a stack is shown in Figure 2-15(a) on the facing page.

In the other set of experiments, the layers with an odd number (1, 3 and 5) were coated with solutions containing TiO_2 nanoparticles with various concentrations reaching from 21.9 - 180.4 g/l (see Table 2.2 on page 33 for further details) and the layers containing SiO_2 nanoparticles were always spin-coated with the same concentration. A sketch of a stack is shown in Figure 2-15(b) on the facing page. This set of experiments is referred to as stackcal.

In Figure 2-15(c) the concentration of the SiO_2 nanoparticles in solution was varied. The non-uniformity matches the one in in the previous experiments. The void space of the TiO_2 layers is constant at around 33 %. The void space of the SiO_2 layers, however, drops significantly at concentrations of 40 g/l and lower. This might be an evidence for slightly smaller TiO_2 particles

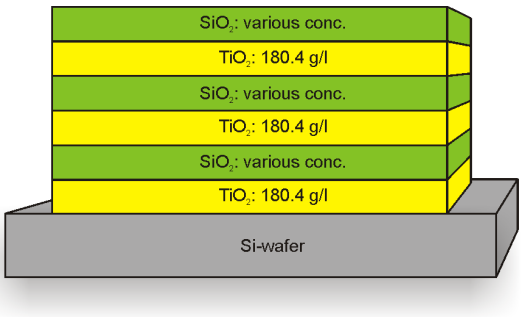

(a) Sketch of the sample setup for Stackcal of silica.

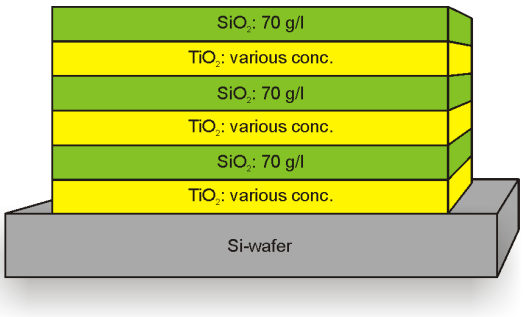

(b) Sketch of the sample setup for Stackcal of TiO_2.

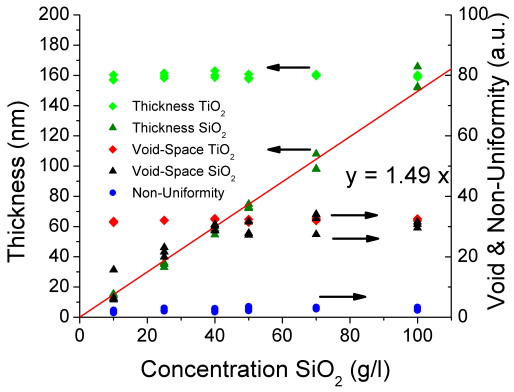

(c) Ellipsometric data for stackcal experiments, where the TiO_2 concentration was constant and the SiO_2 concentration was varied.

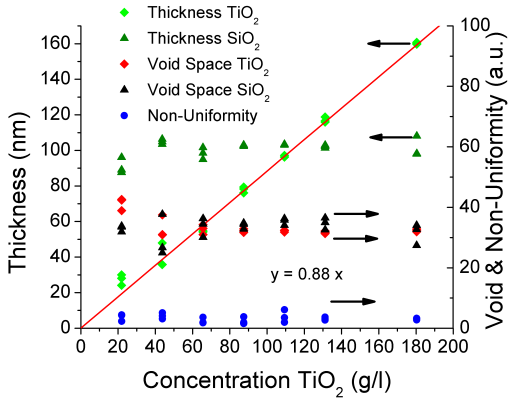

(d) Ellipsometric data for stackcal experiments, where the TiO_2 concentration was varied and the SiO_2 concentration was kept constant.

Figure 2-15.: Sketch of the setup for the stackcal samples and the results from the ellipsometric characterization. The linear regression yields an $R^2 = 0.9998$ and $R^2 = 0.9995$ for SiO_2 and TiO_2, respectively.

that interpenetrate the layers of the SiO_2 nanoparticles. The interpenetration should also occur when the SiO_2 layers are thicker, though, this cannot be observed using ellipsometry since the interpenetration seems to occur only in the first couple of nanometers of each layer. When the layers of SiO_2 are thicker this effect does not contribute as much to the overall void space.

The increase of the layer thickness of the SiO_2 layers follows a linear behavior which indicates that there is only very little influence of the previous layers on the thickness of the SiO_2 layers. This gets also verified by the thickness of the TiO_2 layers which stays constant at around 160 nm. This is coherent with the thickness obtained from the *thickcal* experiments (see Figure 2-13(c) on page 22). The increase in thickness was fitted by linear regression through the origin, yielding a slope of 1.49 nm/(g/l), which is in good agreement with the slope observed in the *thickcal* set of experiments (compare for Figure 2-13(b)) which was 1.47 nm/(g/l). There is no evidence of layers with different nanomaterials influencing the thickness of each other (except for very thin layers).

In Figure 2-15(d), where the concentration of the TiO_2 nanoparticles was varied, the non-uniformity matches the one observed in the previous experiments. The void space of the SiO_2 layers stays constant at around 35 %. The void space of the TiO_2 layers is slightly higher at the lowest concentration, which is coherent with the observations made in the previous experiment (compare for Figure 2-15(c) on the preceding page). This increase in void space is attributed to the TiO_2 particles that are trapped in the SiO_2 layers, and therefore, leave empty spaces in the TiO_2 layers. Again, this effect cannot be observed at higher concentrations since in those cases the layers are much thicker.

The increase in thickness in the TiO_2 layers follows a linear behavior, which shows that there is little to no influence of the SiO_2 layers on the thickness of the TiO_2 layers. The constant thickness of the SiO_2 layers at around 100 nm verify this result. Linear regression of the thickness of the TiO_2 layers through the origin yields a slope of 0.89 nm/(g/l), which is in good

agreement with the slope extracted from the thickcal set of experiments (see Figure 2-13(c) on page 22) which was 0.90 nm/(g/l).

The data collected in this section shows that the layers out of SiO_2 and TiO_2 do not influence the thickness of each other in multi-layer spin-coating (assuming a layer thickness that is high enough). Furthermore, with the data collected from the linear regressions it is now possible to calculate the thickness of a spin-coated nanoparticular layer, which is important when it comes to design and built-up of Bragg stacks. With the knowledge about how to build layers with a controlled thickness, tailor-made Bragg stacks can be produced with the stop band at the desired spectral region. The results of this section are summarized in Table A.1 on page 79 in the appendix.

2.2.4. Spin-Coating of Bragg Stacks

This section describes how to produce tailor-made Bragg stacks. The samples were characterized using UV/VIS absorption spectroscopy[3] and SEM.

To demonstrate the increase in absorbance of the fundamental reflex with an increasing number of bilayers (BL), a piranha-cleaned glass substrate was spin-coated with alternating layers of TiO_2 and SiO_2, starting with TiO_2. The solutions had a concentration of 67 g/l and 113 g/l for SiO_2 and TiO_2, respectively. After each layer, the sample was subjected to 450 °C for 1 h. Every 2 BL (four layers in total) after the calcination step, an absorption spectrum was collected (see Figure 2-16 on the next page). While the spectrum for the sample with only two bilayers had no significant reflex, the 4 BL stack already shows a prominent reflex at 520 nm. This reflex

[3] For the reflectant mode in UV/VIS-spectroscopy a reference is needed that exhibits 100 % reflectance. However, since there is no such substrate (if the reference is less than 100 %, the spectra gets squeezed at the top), useful information gets lost.

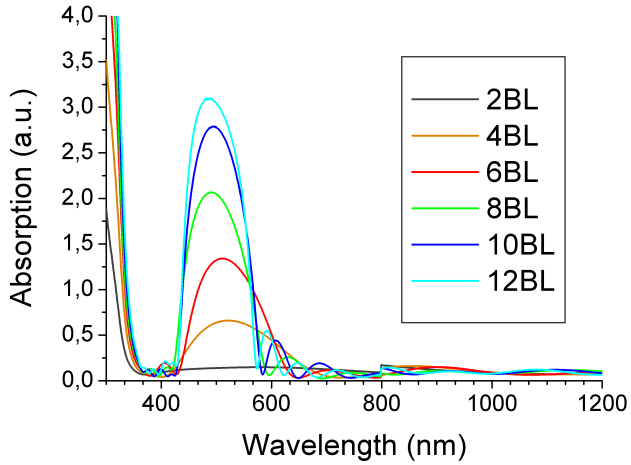

Figure 2-16.: Absorption spectra of a Bragg stack coated with 67 g/l SiO_2 and 113 g/l TiO_2 solution. The increase in absorbance with increased number of bilayers is demonstrated.

from the 4 BL stack is still very broad. When the number of bilayers is increased, the full width at half maximum (FWHM) gets smaller and the intensity in absorption increases. The peak from the 12-BL sample is shifted to 486 nm. This might be attributed to a sintering process that occurs after multiple calcination steps during which the individual layers get thinner, leading to a blue-shift of the fundamental reflex.

To demonstrate the good coverage of the complete VIS-range, three Bragg stacks with three different layer thicknesses were coated. The concentrations of the spin-coating solutions were as follows:

	conc. silica (g/l)	**conc. titania (g/l)**
01-TS-70	47	79
01-TS-100	67	113
01-TS-140	94	158

The standard spin-coating protocol as given in Section 2.3.4 was used. A total of 12 BL was

coated onto the glass substrate.

The resulting spectra of the 12 BL stacks are shown in Figure 2-17(a) with the correspondant optical images in Figure 2-17(b). The graph shows the excellent coverage of the complete optical spectrum from UV to NIR. All reflexes have very small full width at half maximum and the maximum has an absorption of 2.9 - 3. The sample named 01-TS-140 shows one additional peak at 370 nm. This reflex is a higher order reflex (second harmonic), which proves the high quality of the Bragg stacks.

To show that an increased BL-thickness leads to a red shift of the fundamental reflex, cross-section SEM images of the stacks (see Figure 2-17(a) on the following page), were taken. In the resulting SEM images, SiO_2 and TiO_2 are easy to differentiate by their contrast. Since the TiO_2 layers have a large scattering cross-section due to their higher mean atomic number, they appear lighter than the SiO_2 layers. The BL thickness in the 01-TS-70, 01-TS-100 and 01-TS-140 samples are 119, 163 and 212 nm in average, respectively. This shows that the red-shift in the absorbance maxima can be attributed to an increased BL thickness, which is coherent with Equation 1.1.

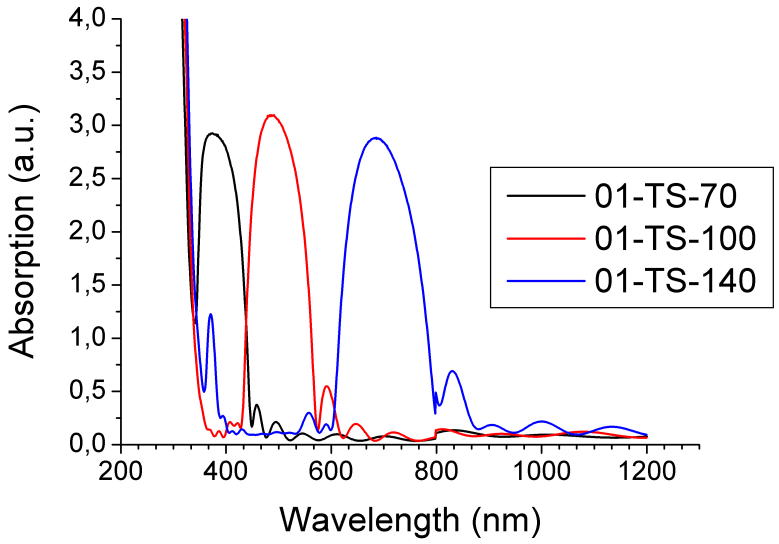

(a) Absorption spectra.

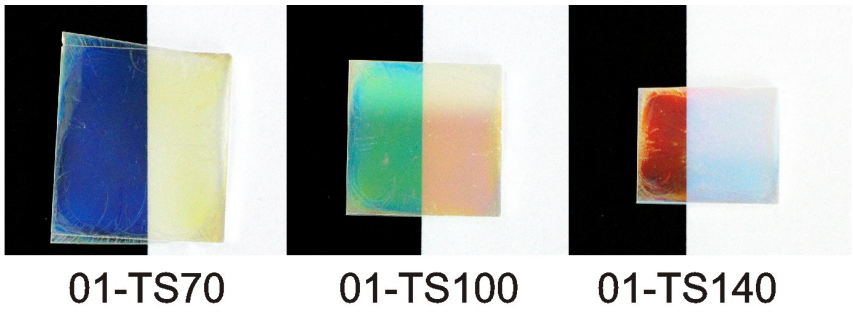

(b) Optical image.

Figure 2-17.: Absorption spectra of the samples 01-TS-70, 01-TS-100 and 01-TS-140. This demonstrates the good coverage of the complete optical spectrum. (b) The optical images show the transmitted color (white background) and the reflected color (black background) of the samples.

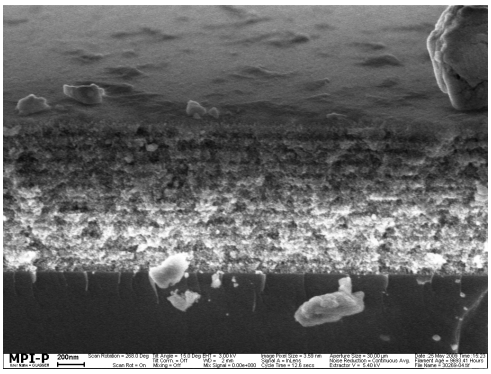

(a) 01-TS-70.

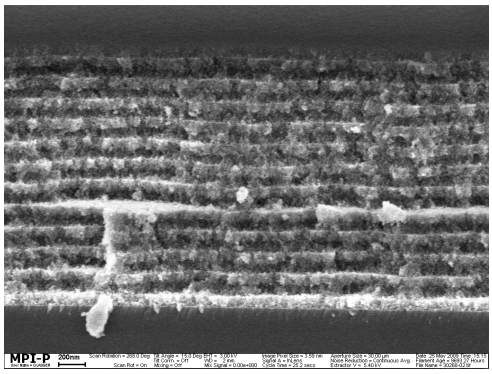

(b) 01-TS-100.

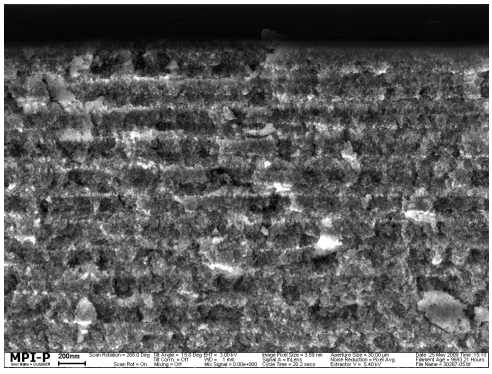

(c) 01-TS-140

Figure 2-18.: SEM-images of the stacks shown in the absorption spectra above.

2.3. Experimental

2.3.1. DHCA-Functionalized Titania Nanoparticles

20.6 ml of Titanium(IV) isopropoxide (Aldrich) were rapidly added to 37 ml of deionized water (18.3 MΩ) and stirred for 1 hour in order to destroy larger agglomerates. The white precipitate that had formed was filtered out by a Buchner funnel and washed with 100 ml of water. The white solid was transferred into a Teflon lined stainless-steel autoclave, 12.8 ml of a 0.56 M tetramethylammonium hydroxide (TMAOH, Aldrich) and 0.96 g of 3,4-dihydroxyhydrocinnamic acid (DHCA, Aldrich) were added and the suspension was mixed thoroughly. Then, the autoclave was placed into an oven for 6 hours at 120 °C to achieve peptization. After this step, the autoclave was subjected to 195 °C for 4.5 hours to achieve particle growth, yielding a dark-red solution with a strong fishy odor. This smell might result from the following reaction:

$$N(CH_3)_4^+ + H_2O \longrightarrow HN^+(CH_3)_3 + CH_3OH$$

In order to determine the concentration of nanoparticles in the solution, 2 ml of the final solution were placed in a crucible that was subjected to 450 °C over night. The concentration was found by difference in weight between the empty crucible and the one with the pyrolyzed nanoparticles.

2.3.2. Cleaning of Substrates

This procedure can be used for either Si-wafers or glass slides. First the substrate was cut into pieces of about 2 x 2 cm^2. These pieces were then immersed for 2 hours into a freshly prepared piranha-solution consisting of one part of hydrogen peroxide (Acros) and two parts of concentrated sulfuric acid (Aldrich). Afterwards, the solution was discarded and the substrates were washed with water repeatedly. Then, the pieces were rinsed thoroughly with Ethanol (Carl Roth) and dried in a stream of dry nitrogen. The samples were subjected to thermal treatment

at 450 °C in air for 1 hour to further grow the oxide layer on the surface of the Si-wafers and thereby hydrophilize the surface.

2.3.3. Composition of the Used Coating Solutions for the Ellipsometric Characterization

The TiO_2 solutions were diluted starting from a 180.4 g/l solution. The SiO_2 solutions were diluted starting from a 30 % LUDOX®AS-30 solution using a 14 % ammonium hydroxide solution (Aldrich).

Table 2.2.: Concentrations and used volumes for the Titania solutions.

Concentration / g/l	Volume / ml	SDS / μl	NH_3 / ml	TiO_2/ ml
180.4	5	50	0.00	5.00
131.2	5	50	1.36	3.64
109.3	5	50	1.97	3.03
87.5	5	50	2.58	2.42
65.5	5	50	3.18	1.82
43.7	5	50	3.79	1.21
21.9	5	50	4.39	0.61

Table 2.3.: Concentrations and used volumes for the Silica solutions.

Concentration / g/l	Volume / ml	SDS / μl	NH_3 / ml	SiO_2 / ml
150	5	50	2.92	2.08
100	5	50	3.61	1.39
70	5	50	4.03	0.97
50	5	50	4.31	0.69
40	5	50	4.44	0.56
25	5	50	4.65	0.35
10	5	50	4.86	0.14

2.3.4. Spin-Coating Protocol

First the spin-coater was set to the desired parameters. Most of the time, the following parameters were used:

Speed	5000 rpm
Acceleration	5040 rpm/s
Time	20 s

The thoroughly cleaned sample (see Section 2.3.2 on page 32) was blown off with dry nitrogen to get rid of attached dust particles since they are the main sources of comets. The substrate was then carefully placed at the very center of the device and fixed by applying of vacuum. The spin-coating solution, diluted to the desired concentration containing 1000 ppm SDS, was filtered using a 0.2 μm PTFE syringe filter directly onto the substrate until the whole substrate was covered. The cover of the spin-coater was closed and the process was started[4]. After the process was finished, the sample was placed into a petri dish and was subjected to heat treatment for at least 1 h at 450 °C in air. After the sample had cooled down, the subsequent layers were

[4]This should happen as fast as possible since longer duration of the liquid on the substrate leads to evaporation of the solvent, and therefore, a higher particle concentration.

spin-coated.

2.3.5. Instrumentation

The used spin-coater was a Laurell WS-400-6NPP-LITE. UV/VIS spectra were collected using a Cary 55 UV/VIS-NIR spectrometer with Cary WinUV v. 3.0 as software. SEM images were taken using a Zeiss Gemini 1530 and a Hitachi S-5200.

3. Photonic-Crystal Dye Laser

Corresponding publication: Francesco Scotognella, Daniel P. Puzzo, Angelo Monguzzi, Diederik S. Wiersma, Dominik Maschke, Riccardo Tubino, Geoffrey A. Ozin, Nanoparticle One-Dimensional Photonic-Crystal Dye Laser, *Small* **2009**, 5(18), 2048 - 2052.

3.1. Introduction

Photonic crystals are well known for their bright color that originates from their photonic band gap. In this gap, photons with a certain energy can neither pass through nor get absorbed. They get reflected[23–30].

Additionally to the effect of a photonic band gap, there also exists a pronounced maximum in the photonic density of states (DOS) near the band edge. At these maxima of the DOS, bands exhibit small slopes. Thus, one observes slow photons[31]. This effect has mostly been analyzed in opals and inverse opals[9, 32–35], where it can be used to amplify photooxidation. However, this effect also occurs in Bragg stacks.

The optical dispersion in Figure 3-1 on the following page corresponds to a 12 Bilayer stack made out of titania and silica with a modeled thickness of 280 nm. The spectrum and the phase were computed using the software WinCPC version 0.5a written by Georg v. Freymann. The

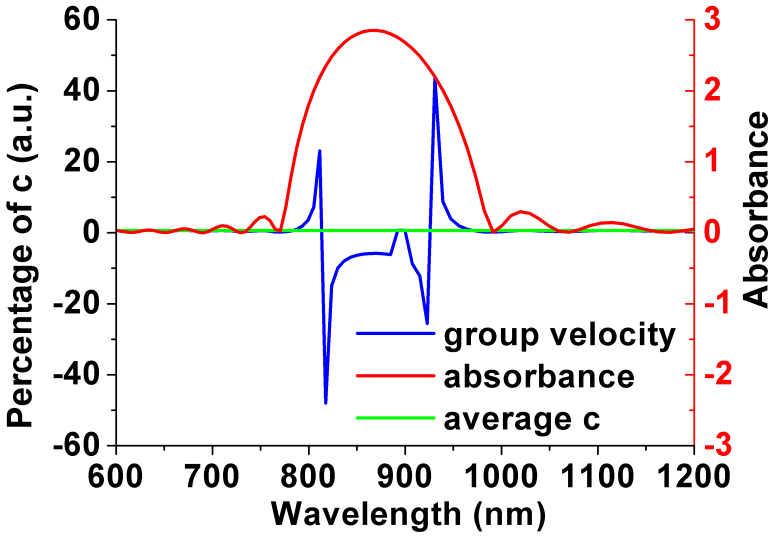

Figure 3-1.: Calculated Absorbance spectrum and group velocity of a 12 BL photonic crystal. The BL-thickness is 280 nm.

group velocity, v_g, was derived using equation 3.1 from Mihi et al.[36], solved for $\upsilon_g(\omega)$

$$\frac{\partial \Delta\phi(\omega)}{\partial \omega} = L\left(\frac{\partial k_{eff}(\omega)}{\partial \omega} - \frac{\partial k_t}{\partial \omega}\right) = L\left(\frac{1}{\upsilon_g(\omega)} - \frac{n_t}{c}\right) \tag{3.1}$$

The variables are described as:

ϕ	phase
L	total length of the PC
k_{eff}	effective wave vector
υ_g	group velocity of light
n_t	average refractive index
c	speed of light in vacuum

The absorbance spectrum, depicted in red shows a prominent reflection at approximately 860 nm. The group velocity, plotted as a blue line exhibits minima at 817 and 923 nm. It is plotted as percentage of c. The increased speed of light at 811 and 931 nm are due to simplifications in the model and do not represent physical facts. This picture shows that near the band-edge the

group velocity is smallest, and therefore, the DOS is largest.

The increased DOS at the band-edge can be used to develop a surface emitting feedback laser, as proposed by Komikado et al.[37]. The laser oscillates at the band-edge, where the photon density is enhanced. In addition to the cavity, provided by the Bragg stack, an active dye is needed that can be excited by a pump.

In this work rhodamin 6G (R6G) (Figure 3-2) was used as dye. This dye has a high molar absorption coefficient of about 1.2 L $mol^{-1}cm^{-1}$ at 532 nm. The photoluminescence quantum yield is 0.86 at room temperature. R6G is well known for its high photostability and low cost. It has an optical gain range from 550 - 600 nm. The maximum in optical gain lies at 570 nm[38, 39]. Most important for this work is the cationic character of R6G. This leads to a favorable interaction with the negatively charged surfaces of SiO_2 and TiO_2, yielding a high dye loading of the porous Bragg stack.

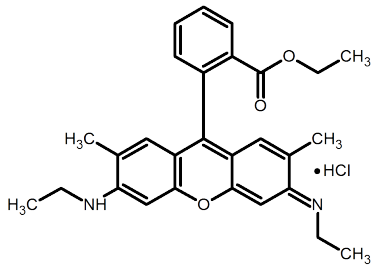

Figure 3-2.: Rhodamin 6G.

3.2. Results and Discussion

The position of the stop band can be estimated using the Bragg-Snell diffraction law.

$$m\lambda = 2(n_H h_H + n_L h_L) \tag{3.2}$$

Where h_L and h_H are the thicknesses of the low and the high refractive index layers and n_L and n_H are the respective refractive indices. From equation 3.2 it can be derived that the position of the stop-band can be manipulated throughout the VIS spectrum by simply manipulating the thickness of the individual layers. This is easily achieved by adjusting the concentration of the coating solutions. The intensity of the Bragg reflection and the DOS can be varied by adjusting the number of bilayers.

3.2.1. Preparation of the Sample

In order to achieve a high DOS, the desired Bragg stack has to consist of many bilayers. In this case a 12 BL stack was used since it shows a significant increase in the DOS at the band edge, and it is still possible to produce this Bragg stack in a reasonable amount of time. For this purpose the method described in Section 2 on page 7 was chosen. The concentrations of the coating solutions were as follows:

silica	70 g/l
titania	120 g/l

The absorbance spectrum of the used Bragg stack is shown in Figure 3-3 on the next page. The stack has a strong absorption maximum at roughly 608 nm. The maximum has a total width ranging from about 500 - 700 nm. Since the nanoparticles are transparent and do not scatter light at this wavelength, this spectrum is totally due to the photonic band structure and shows a real photonic band gap. This stack is well suited for the use with R6G.

The dye was adsorbed by immersing the complete stack in a 10^{-3} M rhodamin 6G (Exciton) solution in water for 24 hours. For a similar 11 BL Bragg stack coated by xxx prepared with a slightly different titania sol, SEM images and confocal images were taken to analyze the

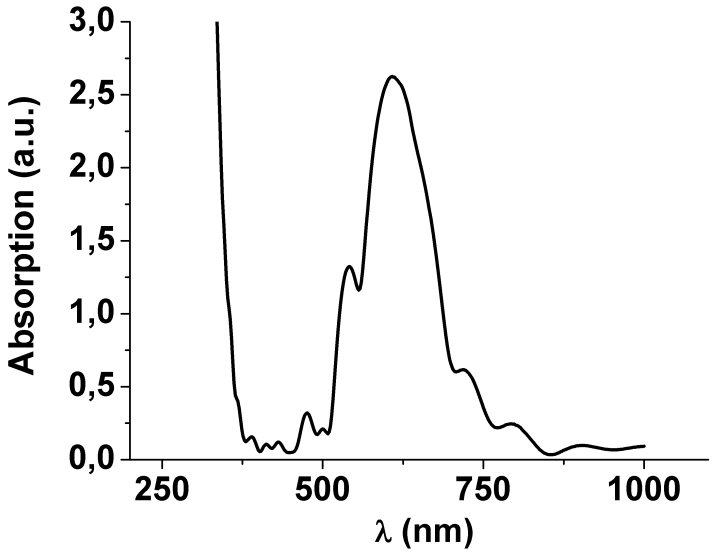

Figure 3-3.: Absorbance spectrum of the used Bragg stack. The absorption maximum lies at 608 nm.

structure of the Bragg stack and to verify a complete dye-loading[1]. The thicknesses derived from the stack shown in Figure 3-4(a) and 3-4(b) are in good agreement to each other.

3.2.2. Measurement of Lasing Behavior

The detailed instrumental setup for the photoluminescence (PL) measurement can be found in Section 3.4.2 on page 45. As depicted in Figure 3-5(a) on the next page, the 532 nm laser pump hits the sample at a slightly oblique angle with respect to its normal. The stimulated emission from the dye exits the structure perpendicular to the sample surface, in the same direction as the periodicity of the stack. All experiments were carried out in ambient atmosphere. The pulse energy density in this experiment has been varied between 0.1 and 0.6 J/cm^2 to avoid destruction of the sample. The pump beam was focused on a spot of roughly 0.3 mm in diameter. A photograph of the sample can be seen in Figure 3-5(b) on the following page.

[1]Unfortunately, I had to leave Toronto right when this project started, so xxx completed this project with xxx. The description of the images states when the stack was coated by xxx.

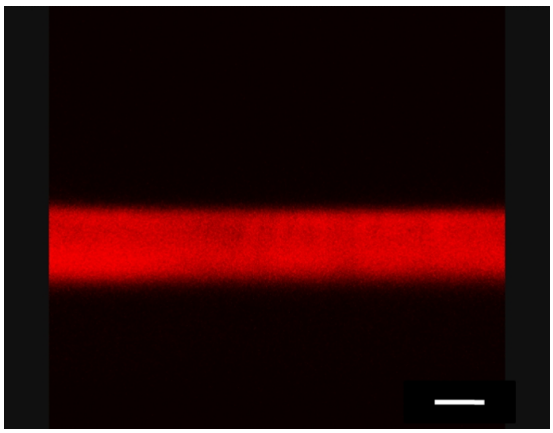

(a) Scalebar: 1.5 μm

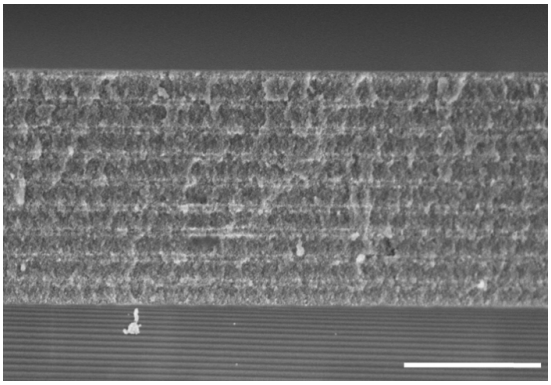

(b) Scale bar: 1 μm

Figure 3-4.: Cross-section confocal image and cross-section SEM image of the Bragg stack coated by xxx.

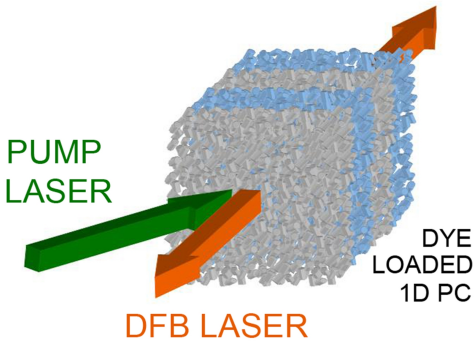

(a) Schematic of the lasing setup.

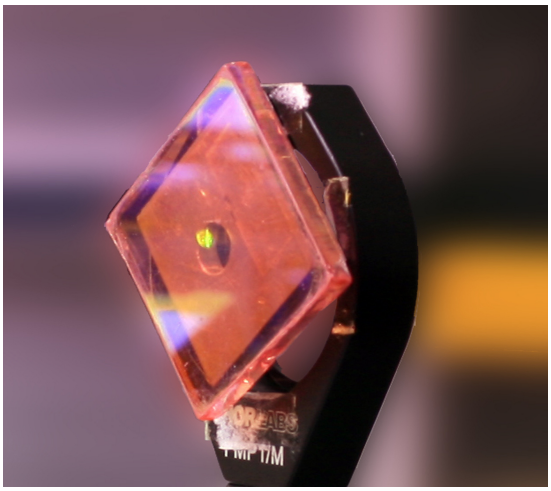

(b) Image of the sample.

Figure 3-5.: Schematic for the setup of the PL-investigations and image of the sample excited at 532 nm at 40 μJ/cm^2.

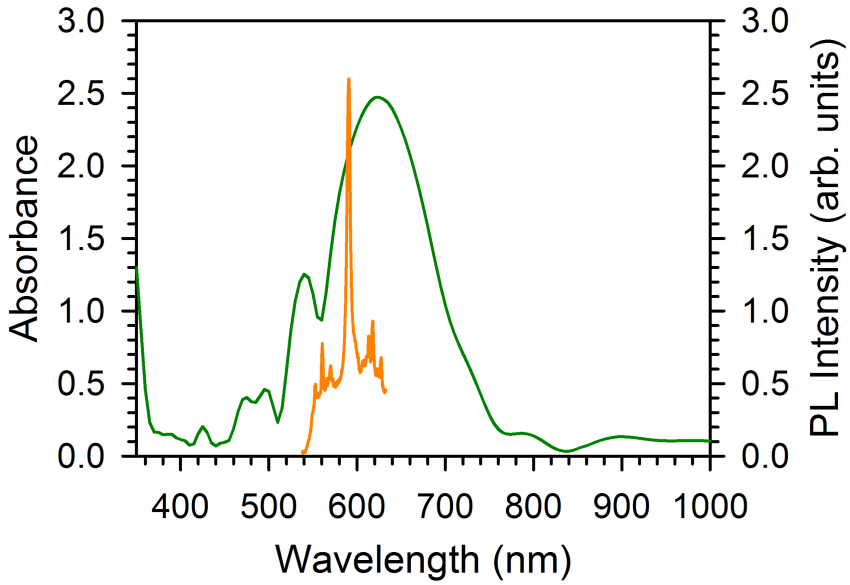

Figure 3-6.: Reflectance spectrum of the Bragg stack (green line) and PL spectrum of the dye (orange line) excited at 530 nm with a power density of 560 mJ/cm^2.

When the sample gets excited with a pump laser beam of 560 mJ/cm^2, a narrow emission peak is clearly detectable at 590 nm, near the blue-edge of the stop band (see Figure 3-6). The shape of the emission matches the gain range of an R6G spontaneous emission. Since R6G absorbs the maximum of the laser emission efficiency at 570 nm, the PL peak at 590 nm has to be due to the Bragg stack architecture[40].

In most lasing systems, a threshold excitation energy density exist to obtain the stimulated emission. This phenomenon was analyzed by exciting the sample with different energy densities (see Figure 3-7(a)). The PL-spectrum below the excitation threshold value (green) is 15 times magnified. It shows a broadband emission of R6G that is slightly shaped by the photonic band gap. The PL-spectrum above the excitation threshold value exhibits a narrow line (approx. 6 nm).

In Figure 3-7(b) on the following page the spectral shape of the stimulated emission and rel-

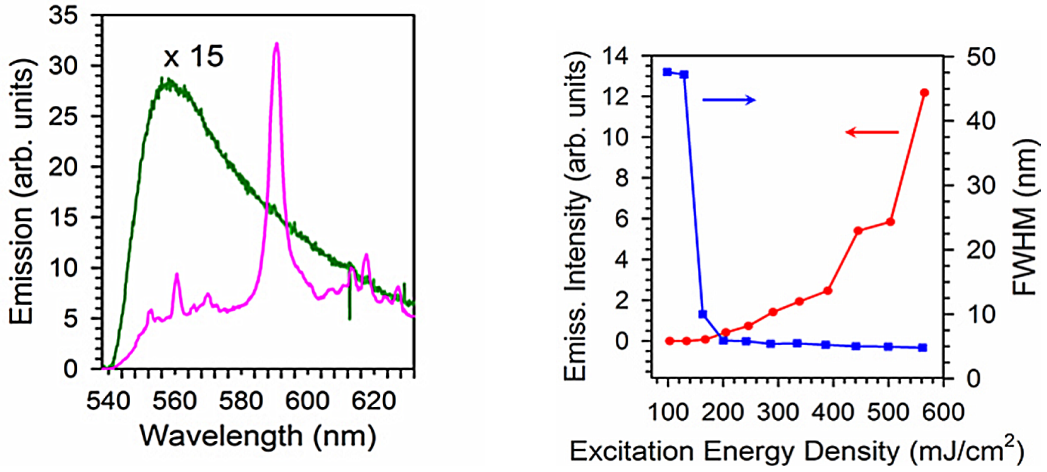

(a) PL-spectrum under (green) and over (pink) the excitation threshold.

(b) PL intensity (red) and peak FWHM at 590 nm (blue) as a function of the excitation energy density at 532 nm.

Figure 3-7.: Analysis of the excitation threshold.

ative intensity have been analyzed as a function of the excitation energy. The red line indicates the emission intensity at 590 nm as a function of the excitation density of the pump laser. By increasing the excitation pump density, the emission peak density is strongly enhanced. Simultaneously the full width at half maximum (FWHM, blue line) is decreased. The lasing threshold of this system was determined to be approximately 170 mJ/cm^2.

3.3. Conclusion

The Bragg stacks described in this work exhibit a FWHM that is comparable with the literature[41]. We could demonstrate the first example of a DFB-laser based on a Bragg stack made out of nanoparticles and an organic dye. The system shows a stimulated emission at the blue edge of the stop band.

3.4. Experimental

3.4.1. Preparation of the Bragg Stack

The preparation of the Bragg stack used in this section followed the procedure described in Section 2.3 on page 32. The concentration of the coating solution was 70 and 120 g/l for SiO_2 and TiO_2, respectively.

3.4.2. Instrumentation

The spin coater was a Laurell WS-400A-6NPP/LITE. Absorption spectra in the range 300 to 1000 nm were collected with a Cary Varian 50 spectrophotometer (bandwidth of 1 nm). HRSEM was performed using a Hitachi S-5200 (10 - 15 kV, 15 mA). As light source the second harmonic of 1064 nm Nd:YAG TEM00 pulsed laser (Quanta System, repetition rate 1 Hz, pulse duration 5 ns) was used. Spectra were recorded by a nitrogen cooled CCD (Spex 2000) coupled with a polychromator (Triax 190 from J-Horiba), with a bandpass of 0.2 nm for signal detection. Excitation laser light was removed by using a proper notch filter (Edmund Optics).

4. Electrochromic Bragg Stacks

4.1. Introduction

4.1.1. Motivation

Photonic crystals are known in nature as well as in engineering. The building blocks for Bragg stacks, i.e. 1D photonic crystals, are high and low refractive index materials. They are usually electronically inert and inherently colorless, which makes the fabrication of Bragg stacks with static and dynamic tunability challenging. To date only a few examples of tunable Bragg stacks have been reported: Porous silicon stacks[15, 42–45], mesoporous silica and titania stacks[46, 47], as well as layer-by-layer assembled stacks composed of silica and titania[48].

Although electronic tunability has been demonstrated on a 3-D photonic crystal (opal)[7], hitherto, to the best of our knowledge, there exists no nanoporous Bragg stack that can be altered electronically.

This work shows that it is possible to attach an electrochromic WO_3 layer to a Bragg stack. The function of the stack is not influenced by the electrochromic layer; however the Bragg stack on top of the electrochromic layer influences the response time and the contrast ratio of the coloration/bleaching processes. This work demonstrates that it is possible to built up multifunctional Bragg stacks by combining two devices.

4.1.2. Electrochromism

Electrochromism describes the property of a material to change color when an electric bias is applied. Electrochromic devices are already used in every-day applications. They can be found in smart windows[49, 50], which can be darkened by applying an electric bias. Car manufacturers use them to automatically darken a rear mirror when hit by bright light. They can be utilized to save energy by integrating smart windows in state-of-the-art buildings.

The most widely used material is tungsten(VI) oxide (WO_3)[51]. The simple reaction that lies behind the coloration process can be described as:

$$WO_3 + xM^+ + xe^- \longrightarrow M_xWO_3$$

with $M^+ = H^+$, Li^+, Na^+ and K^+. Thus, when the transparent WO_3 film incorporates electrons and charge-balancing ions, its properties are drastically altered. The WO_3 becomes deep blue.

In a standard cell setup, the WO_3 layer is coated on a transparent conducting oxide (TCO) coated glass such as Fluorine doped tin oxide (FTO) or indium doped tin oxide (ITO) coated glass. The counter electrode is made up from another TCO-coated glass. $LiClO_4$ in propylene carbonate is widely used[52, 53] as electrolyte, usually in concentrations ranging from 0.5 to 1 M. A schematic setup of an electrochromic cell is shown in Figure 4-1(a) on the facing page.

In this work a Bragg stack was coated on top of the electrochromic layer (see Figure 4-1(b)). This allows to have the permanent reflection of the Bragg stack at a desired wavelength. To this reflection the broad absorption of the electrochromic layer can be added by applying an electric bias.

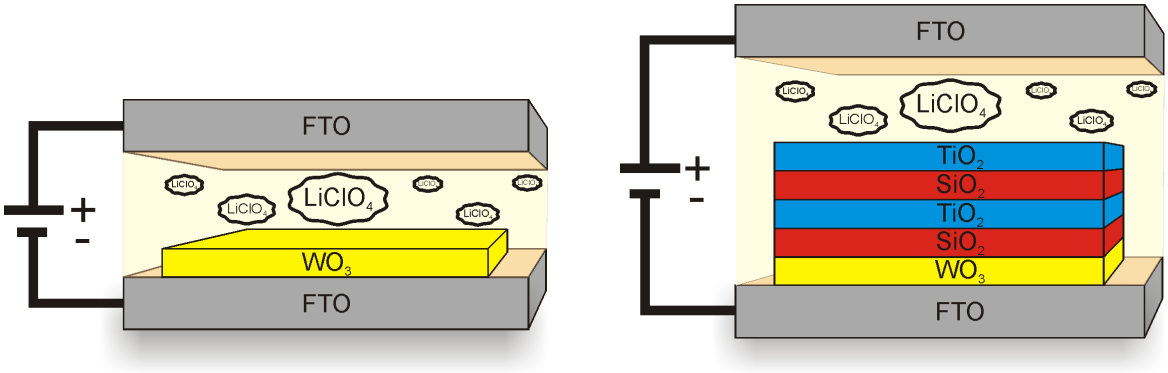

(a) Standard setup of an electrochromic device. The WO_3 layer is attached to FTO-coated glass. A $LiClO_4$ in Propylene carbonate serves as electrolyte.

(b) Schematic design of the devices that were used in the present work. A Bragg stack is attached on-top of the electrochromic layer.

Figure 4-1.: Schematic setup of a standard electrochromic device and the modified device with a Bragg stack on top.

4.2. Results and Discussion

4.2.1. Manufactoring of Bragg Stacks

Figure 4-2(a) on the next page shows a 52 nm thick WO_3 film (as determined by SEM investigation) on silicon after calcination at 450 °C for 1 hour. The film appears to be solid, with very low porosity. It exhibits some minor cracks orthogonal to the surface of the wafer.

In Figures 4-2(b)-(d) Bragg stacks made out of SiO_2 and TiO_2 nanoparticles attached to the WO_3 layer on the bottom of the picture are shown. The tungsten oxide layer below the Bragg stack exhibits a significantly higher porosity than the individual one (see Figure 4-2(a)). This arises from the alkaline ambiance of the solutions used for spin-coating, which leads to a partial dissolution of WO_3. The initial cracks in the WO_3 film (see Figure 4-2(a)) are probably the places where the etching is most severe; as a result, tungsten oxide is dissolved mostly in these areas.

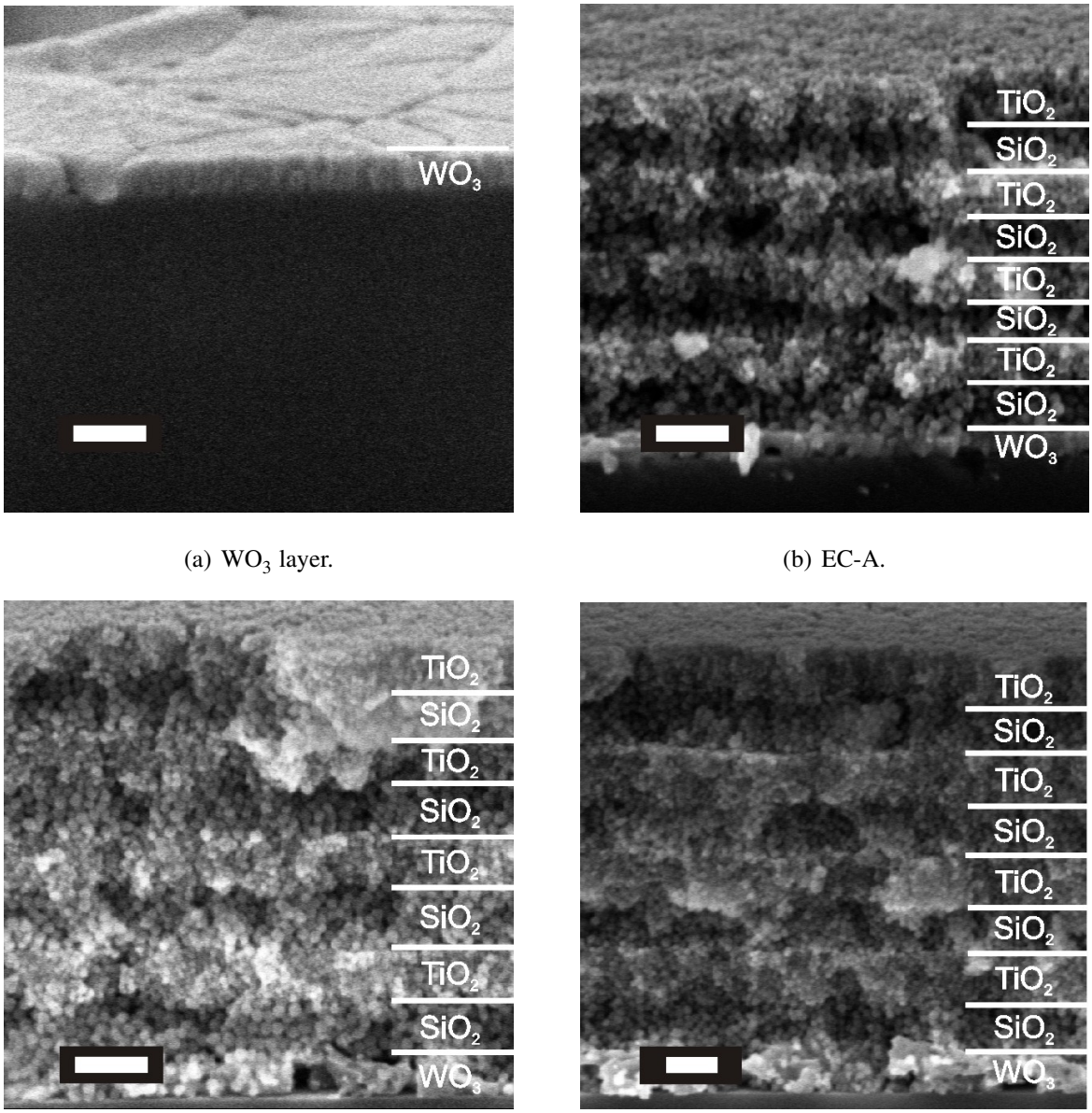

(a) WO_3 layer.

(b) EC-A.

(c) EC-B.

(d) EC-C.

Figure 4-2.: SEM images of a pure WO_3 layer and the Bragg stacks attached to the WO_3 layer. The scale bar is always 100 nm. The different materials are shown in the right-hand side of the picture. All images were taken on Si-wafers.

Albeit the severe increase in defect density in the underlying WO_3 layer, neither the WO_3 nor the final Bragg stack exhibits any significant detachment effects.

The interfaces between SiO_2 and WO_3 as well as between SiO_2 and TiO_2 are very smooth and regular with only a low degree of interpenetration of the particles into the underlying layer. The fact that each layer of the same material has the same thickness as the next is evidence for the quality of the stacks. Details for the preparation of these stacks are given in Table 4.1.

Table 4.1.: Different concentrations used to spin-coat the individual stacks and the thickness of each material from the different stacks. The thickness was derived from cross section SEM pictures.

	conc. SiO_2 g/l	**con. TiO_2 g/l**	**thickness SiO_2 (nm)**	**thickness TiO_2 (nm)**
EC-A	47	79	48	54
EC-B	67	113	81	70
EC-C	94	158	102	100

The thickness of the SiO_2/TiO_2 bilayers determines the position of the fundamental Bragg reflection. By varying the concentration of the nanoparticle solutions, the layer thicknesses of both SiO_2 and TiO_2 can be tuned over a wide range (see Table 4.1). In combination with good interface quality and film homogeneity, this permits a rational tunability of the position of the stop band and ensures high optical quality of the Bragg stacks. Figure 4-3 on the following page shows the UV/VIS absorption spectra of the Bragg stacks. The complete optical spectrum from the UV to the IR range is covered by these spin-coated stacks with absorption maxima at 400 nm, 580 nm and 700 nm for EC-A, EC-B and EC-C, respectively.

4.2.2. Cyclovoltametric Characterization

FTO coated glass sheets coated with pure WO_3 or multilayered WO_3 $(SiO_2/TiO_2)_n$ served as the working electrodes for the cyclic voltammetry experiments. An Ag/AgCl electrode and a Pt

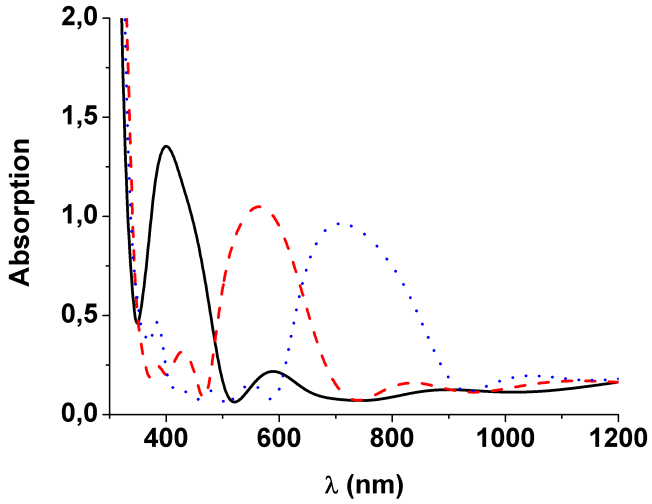

Figure 4-3.: Absorption spectra of the as spin-coated stacks. (-) EC-A, (- -) EC-B and (···) EC-C. All spectra were corrected for a monochromator shift at 800 nm.

electrode were used as reference and counter electrodes, respectively. 1 M $LiClO_4$-PC (propylene carbonate) served as electrolyte. The potential between working and reference electrodes was varied linearly between two given voltage limits at a constant rate, and the current through the working electrode was measured.

Figure 4-4 on the next page shows the cyclovoltammograms of WO_3 (a), EC-A (b), EC-B (c) and EC-C (d) recorded at a scanning rate of 1 mV/s. The two observed reductions at -0,48 V and -0,8 V show the electron uptake reaction with the simultaneous intercalation of x Li^+ ions per WO_3 unit leading to the phase transition from the monoclinic to the tetragonal ($0.05 < x < 0.15$) and further to the cubic phase ($x > 0.15$)[54, 55]. Increasing the voltage leads to discharge; the two phase transitions overlap resulting in only one broadened oxidation step with minimal current density at -0.25 V. These redox processes are observable in pure WO_3 (a) as well as in the stacks ((b)-(d)). The decreasing current density upon increasing stack thickness shows a hindrance but no leaching of the Li^+ ion diffusion from the solution to the WO_3 layer.

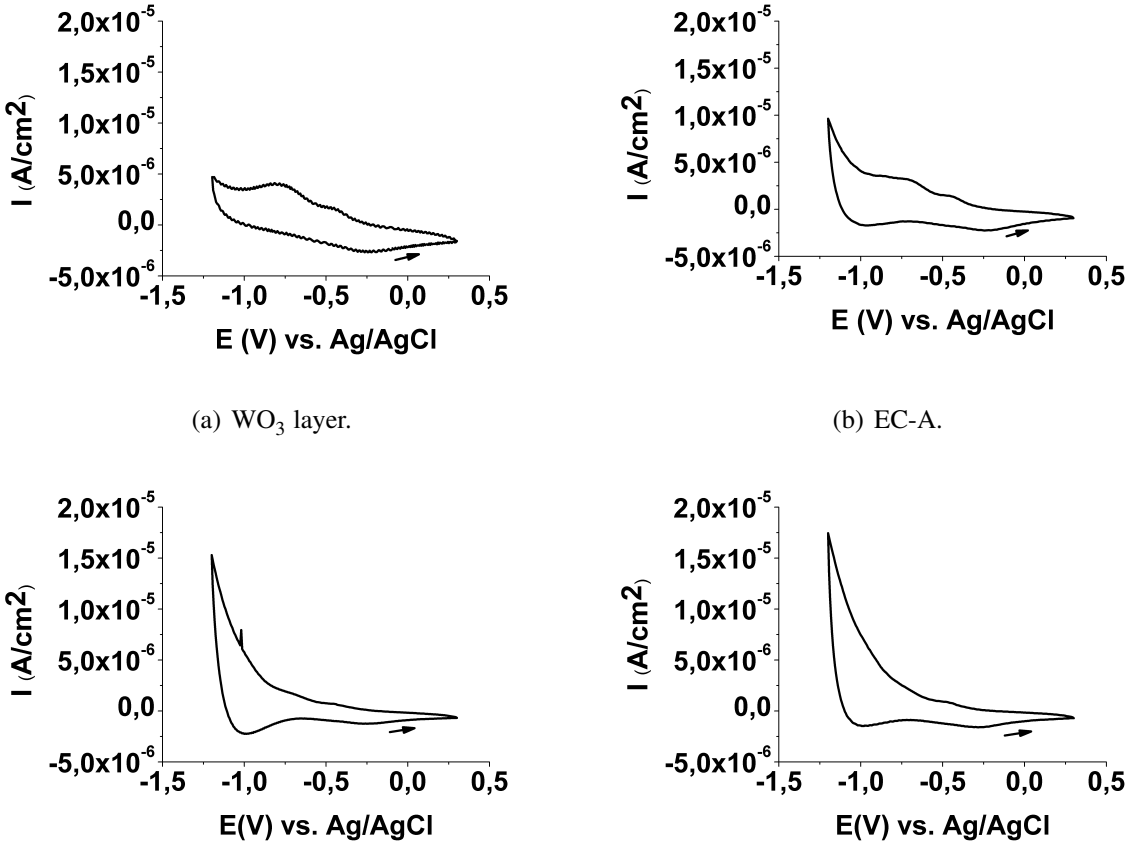

(a) WO_3 layer.

(b) EC-A.

(c) EC-B.

(d) EC-C.

Figure 4-4.: Cyclovoltametric characterization of the Bragg stacks. The scan-rate was 1 mV/s. 1 M $LiClO_4$ in propylene carbonate served as electrolyte.

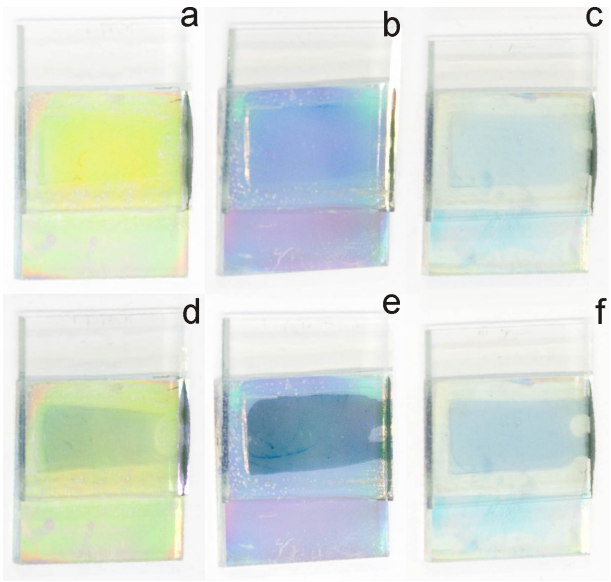

Figure 4-5.: Photographs of the bleached and the colored stacks assembled as cells. The bleached state is always on top (a,b,c) and the colored state is in the bottom (d,e,f). The pictures from left to right are in increasing thickness of the SiO_2/TiO_2 layers. (a) EC-A, (c) EC-B and (e) EC-C.

4.2.3. Optical Characterization of the Stacks

The spin-coated stacks were assembled into cells containing the stack itself on an FTO substrate, an FTO counter electrode and a $LiClO_4$ electrolyte in a sandwich structure. A color change was already observed qualitatively upon a potential bias (see Figure 4-5).

The samples are placed on a white background to make the transmitted color of the stack visible. On a black background the reflected color would be visible but not the blue color of the WO_3. Sample (e) appears most colored, which is due to the fact that the blue transmitted color is enhanced by the tungsten oxide.

In the UV/VIS absorption spectra (see Figure 4-6 on the next page) the blue-colored stacks at a negative bias were compared to the transparent stacks at a positive bias. In order to achieve complete coloration prior to the absorption measurement the samples were subjected to -1.2 V

for 20 min. For the bleaching the current was reversed and the stacks were subjected to +0.3 V for 20 min.

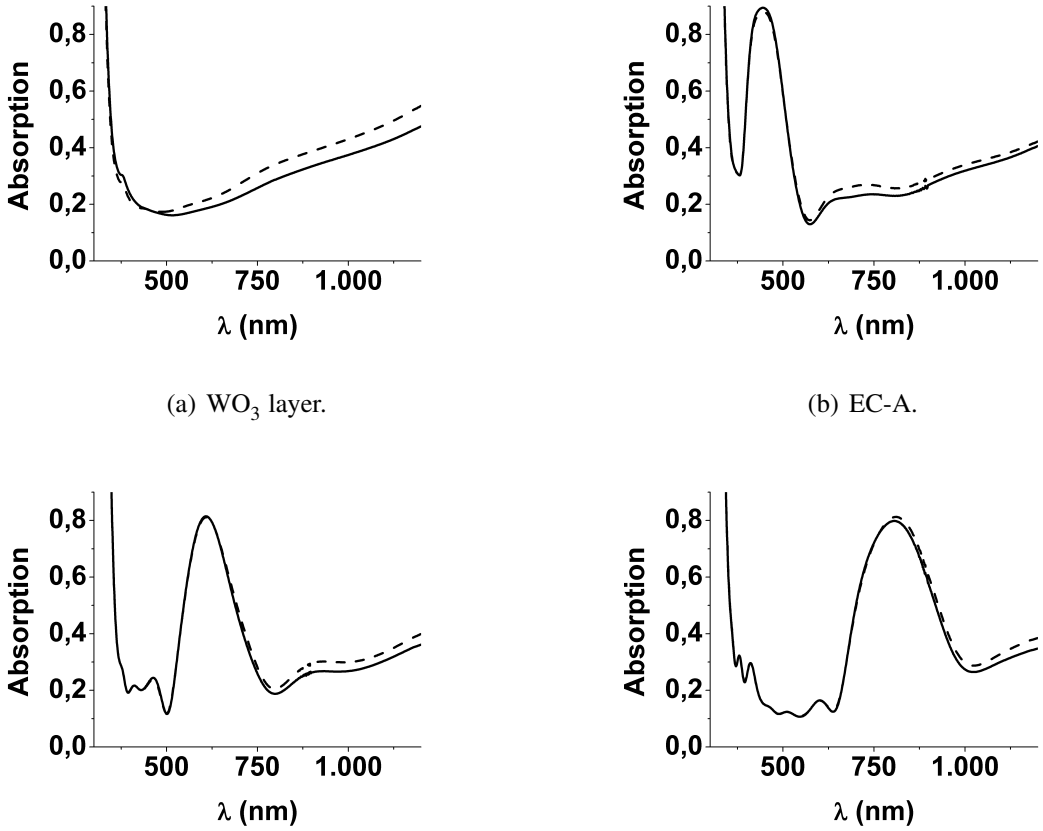

(a) WO_3 layer.

(b) EC-A.

(c) EC-B.

(d) EC-C.

Figure 4-6.: Absorption spectra of the bleached stacks (-) and the blue-colored stacks (- - -). All spectra are corrected for a monochromator shift at 900 nm.

In the spectral region from 300-600 nm, the spectra of the bleached stacks and the spectra of the blue-colored stacks are virtually identical. At higher wavelengths the spectra of the samples at -1.2 V bias exhibit a higher absorption. The coloration of the tungsten oxide influences neither the position nor the intensity of the fundamental Bragg peak. Thus, the WO_3 layer is not part of the photonic crystal. Sample EC-C appears to be red shifted; this, however,

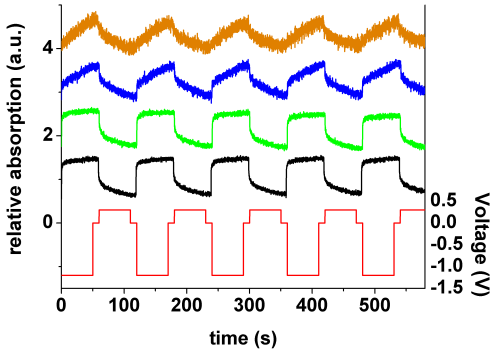

Figure 4-7.: Kinetic investigation of the electrochromic behavior. The absorbance (relative and shifted for a constant value for each sample) was measured while the bias was varied. (a): EC-C, (b) EC-B, (c) EC-A, (d) WO_3 and (e) applied voltage.

is a consequence of the higher absorption of the WO_3 layer and not a photonic effect. The contrast ratio between the negative and the positive bias at 788 nm depends inversely on the overall thickness of the Bragg stack over the electrochromic WO_3 layer. While a pure WO_3 layer exhibits a contrast ratio of 1.192, the latter drops to 1.122, 1.091 and 1.007 for an overall Bragg stack thickness of 408 nm, 604 nm and 808 nm, respectively. As these experiments were conducted with a measurement/induction period of 20 min, these effects cannot be due to the diffusion processes. This can be attributed to the increasing porosity, i.e. the decreasing number of absorption centers, of the electrochromic WO_3 layer upon increasing the thickness of the Bragg stack.

4.2.4. Kinetic Investigation

The samples were subjected to a kinetic investigation where the bias was changed from +0.3 V to -1.2 V and the absorption was measured at a constant wavelength (788 nm, see Figure 4-7) vs. time. The absorption of a pure WO_3 layer increases immediately to 80 % and subsequently rises slowly to 100 % coloration. Upon reversal of the bias the absorption drops by 50 % and then

slowly comes down to 0 %. When a thin TiO_2 and SiO_2 stack is put on top of the WO_3 layer as in Figure 4-7(c), where the absorption of an EC-A stack is shown, the jump immediately after applying the negative voltage is 65 % while the drop upon reversal of the potential is 40 %. With increasing stack thickness, the color changes get less intense and the response time increases.

The effect of a longer response time can be attributed to the increased thickness of the stack on top of the WO_3 layer. The diffusion of the Li^+ ions through the stack is much slower than directly through the electrolyte.

4.3. Conclusion

In summary, it could be shown that it is possible to attach an electrochromic WO_3 layer to a Bragg stack. The function of the stack is not influenced by the electrochromic layer. However, the Bragg stack on top of the electrochromic layer influences the response time and the contrast ratio of the coloration/bleaching processes. This work demonstrates that it is possible to combine these two devices. Future work has to increase the contrast ratio and decrease the response time.

4.4. Experimental

4.4.1. Coating of the WO_3 Layer

In order to coat a thin smooth layer with a spin-coater, the same criteria as mentioned before apply. The solution has to exhibit no agglomeration. Therefore, different synthetic approaches were checked. The most prominent route via peroxotungstic acid[56, 57], where tungsten powder is slowly dissolved in H_2O_2, did not yield a homogeneous film and consequently could not be used.

Another synthetic approach starts by dissolving $WOCl_4$ in isopropanol[58]. This method yields high quality, homogeneous WO_3 films and was used for this project.

In detail, a 5 % dispersion of $WOCl_4$ (Aldrich) in isopropanol was stirred over night until a clear solution was obtained. Then this solution was spin-coated with standard parameters (see Section 2.3.4 on page 34). After this layer was coated, the sample was subjected to heat treatment at 450 °C for 1 hour.

The SiO_2/TiO_2 Bragg stack was spin-coated according to the standard protocol (see Section 2.3.4). The used concentrations are given in Table 4.1. 14 % ammonium hydroxide solution was used to dilute the initial concentrations. 1000 ppm SDS were added to yield good film quality. A total of 4 BL (4 SiO_2 layers and 4 TiO_2 layers, starting with SiO_2) was spin-coated on top of the WO_3 layer. After each cycle, the stack was subjected to 450 °C for 1 hour.

The cells were assembled by melting together the FTO slide with the stack on top and a clean FTO slide as counter electrode with a hot-melt ring SX1170-60 (SOLARONIX). The cells were then filled with a 1 M $LiClO_4$ electrolyte in propylene carbonate by the vacuum-fill technique and sealed with epoxy glue (Epoxy Flüssigmetall 24 G, Toolcraft).

4.4.2. Instrumentation

The used spin-coater was a Laurell WS-400-6NPP-LITE. SEM images were taken using a Zeiss Gemini 1530. UV/VIS spectra were collected using a Cary 55 UV/VIS-NIR spectrometer with Cary WinUV v. 3.0 as software.

The CV-setting was comprised out of the following components:

- Princeton Applied Research Potentiostad/Galvanostad Model 263A, 3 electrode setup
- WO_3 as workingelectrode
- Pt-counterelectrode

- Ag/AgCl-referenceelectrode

The software-package Power Suite v. 2.57 from Advanced Measurement Technology, Inc. 2003; Princeton Applied Research was used to elucidate the data.

5. Phononic Crystals

Corresponding publication: N. Gomopoulos, D. Maschke, C. Y. Koh, E. L. Thomas, W. Tremel, H.-J. Butt and G. Fytas, One-Dimensional Hypersonic Phononic Crystals, *Nano Letters* **2010**, 10(3), 980 - 984.

5.1. Introduction

5.1.1. Phononic Crystals

In the previous chapters, we have seen examples for the utilization of photonic crystals. In this chapter, however, we leave the field of photonics, entering the area of phononics. Phononic crystals are very comparable to photonic crystals, save for the fact that they work with phonons instead of photons.

Just as with photonic crystals, one can realize one-, two-, and three-dimensional phononic crystals. In photonic crystals, the band gap is created by a periodic variation of the refractive index. In phononic crystals however, the band gap is caused by a periodic variation of the density and/or the elastic moduli. In a phononic crystal, a phononic band gap exists in which phonons with a certain frequency cannot exist. These phonons get reflected as do photons in a photonic crystal.

Elastic waves (phonons) can be controlled from sound (10^2-10^4 Hz) to heat (10^{12} Hz), yield-

ing in the construction of numerous designs. Since the designs of a photonic and a phononic crystal are very comparable, it is not surprising that the effort put into the research of photonic crystals greatly influenced the design of phononic crystals and vice versa.

With the tremendous advances made in the field of nanotechnology, specially in the field of thin-film coating, it is now possible to prepare thin layers with high precision in the range of sub 100 nm. These structures can be used to produce 1-D phononic crystals working in the GHz region.

Here we show a new design of a phononic crystal, consisting of a SiO_2/PMMA-hybrid material, with a BL thickness of about 100 nm. This is the first direct experimental example of a band gap in a 1-D phononic crystal in the hypersonic frequency range.

5.1.2. Brillouin Spectroscopy

Photonic structures are relatively easy to characterize, using a simple UV/VIS-spectrometer for example. The direct analysis of phonons is not trivial. With the use of *Brillouin spectroscopy* (BLS), however, it is possible to observe acoustic phonons in a sample. It is a non-destructive and non-contact method to probe the phonon propagation (in microstructures) at hypersonic frequencies. A detailed description of the method can be found in the thesis of xxx[59]. A brief description of the method is given in this work.

The BLS setup is schematically shown in Figure 5-1 on the facing page. BLS uses the photoelastic interaction between incident photons of a single frequency laser beam and sound waves with the wavelength Λ propagating in the medium along a selected direction determined by the scattering geometry (compare for Figure 5-2 on the next page). The wave vector is defined as $q = k_s - k_i$, with k_s and k_i being the wave vector of the scattered and the incident

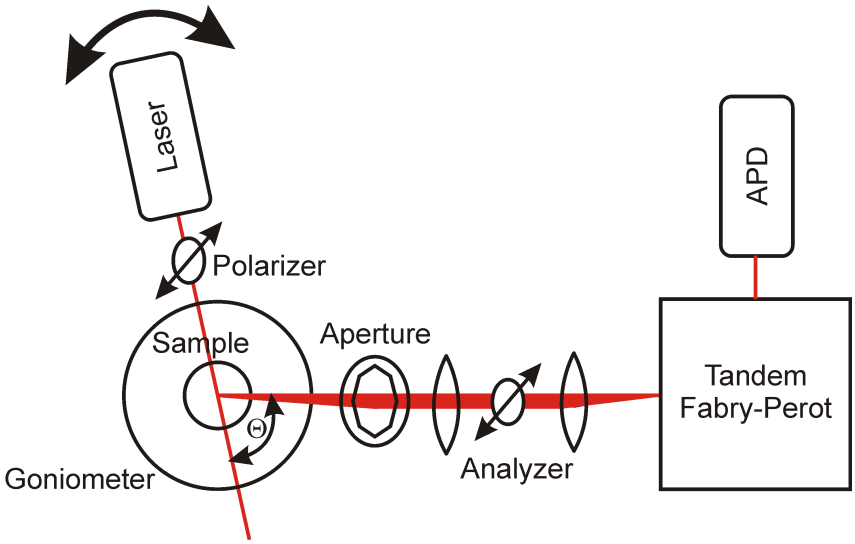

Figure 5-1.: Typical BLS-setup. The sample sits in the center of the goniometer. The scattering angle Θ is adjusted by rotating the laser mounted on the goniometer. The scattered light is collected using two conjugated lenses into an six-pass tandem Fabry-Perot interferometer.

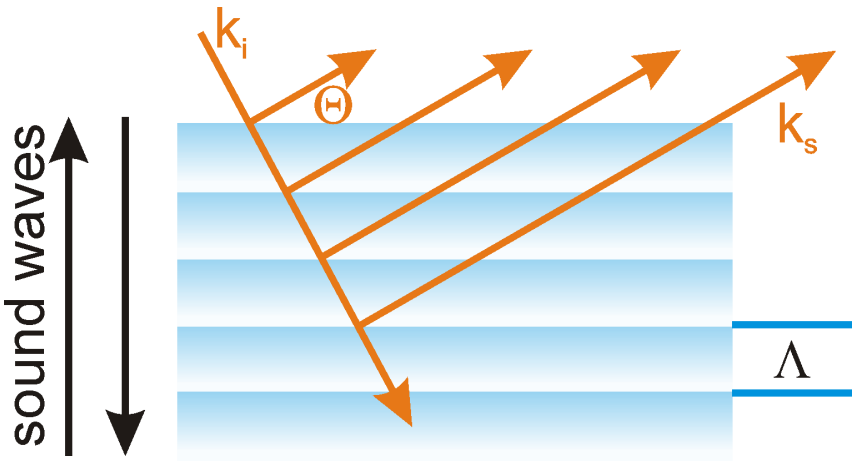

Figure 5-2.: Sound waves in a substrate creating quasi stacks. The incident wave vector is given by k_i, the scattered wave vector is represented by k_s. The wavelength of the sound equals the thickness of the "layers", Λ.

photons. They define the scattering plane. For a homogeneous medium in the size range of the phonon wavelength $2\pi/q$ (effective medium behavior), one finds $q = k$ since the momentum is conserved.

Since the sound wave has the face velocity c, the frequency of the scattered light f_s, as seen by the detector suffers a Doppler shift, which is given by[59]:

$$f_s = f_i \pm \frac{c}{2\pi} q \tag{5.1}$$

or in terms of angular frequency:

$$\omega = \omega_s - \omega_i = \pm cq = \pm ck \tag{5.2}$$

In the geometry used in this work, two different setups for the scattering geometry are possible. In the transmission mode, q lies in the plane parallel to the film surface. Its magnitude is given by $q_{\parallel} = 4\pi/\lambda \sin(\Theta/2)$ (with λ being the wavelength of the incident light and Θ being the scattering angle) and is independent of the refractive index n of the measured medium.

In the reflection geometry, q lies perpendicular to the film surface. Due to light refraction, the accessible $q_{\perp}$ are relatively small[60]. The value of q can be adjusted by adjusting the scattering angle Θ. In hypersonic periodic media, the wave vector q is modified so that $q = k + G$ where G is a reciprocal lattice vector of the crystal.

According to Bloch's theorem[61], phonons with the wave vector k and $k + G$ belong to the same eigenmode in the phononic crystal. Its phononic properties can be revealed by recording its dispersion relation $\omega(q)$.

5.2. Results and Discussion

5.2.1. Sample Preparation

The phononic crystal is realized by a Bragg stack made out of 20 BLs (see Figure 5-3 on the facing page). Silica (LUDOX AS-30, Aldrich) and Poly(methyl methacrylate) (PMMA,

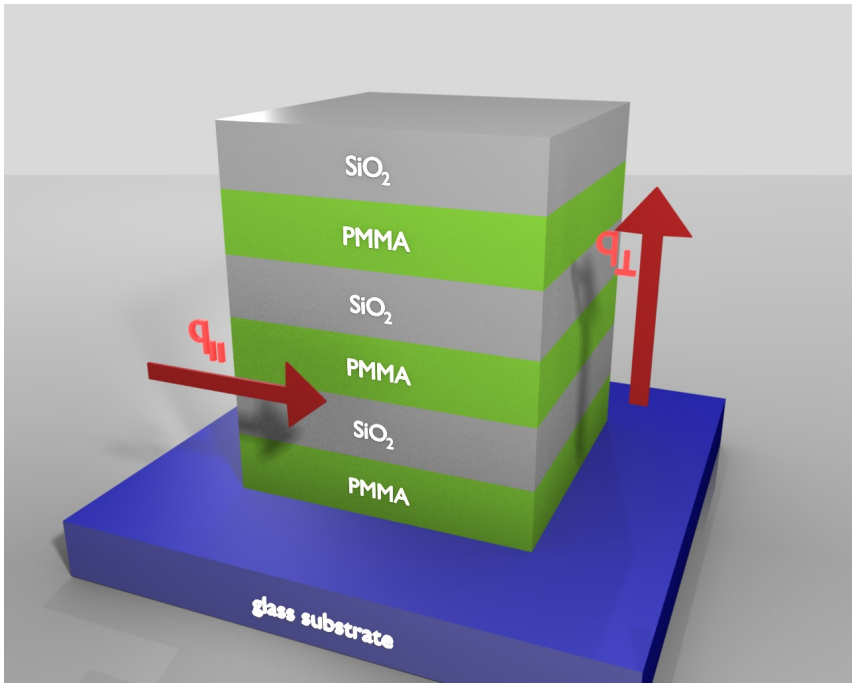

Figure 5-3.: Schematic setup of the sample. And a schematic representation of the scattering geometries.

Acros, M_W: 35 kDa) were used as high and low elastic moduli material, respectively. The stack was spin-coated onto piranha-cleaned glass- and Si-substrates. For the spin-coating of the polymeric-layer, the PMMA was dissolved in toluene and stored as a 10 % (w/v) stock solution. For the spin-coater, the usual settings were used (acceleration: 5040 rpm/s, speed: 5000 rpm and time: 20 s). In order to get information about how the thickness changes with the PMMA concentration, solutions with a concentration of 2, 3, 4, 5 and 6 % (w/v) were spin-coated on Si-wafers, and the thickness was analyzed using a profilometer (Model P16+, KLA-Tencor, Software v. 7.21) (see Figure 5-4 on the next page). The linear regression yields an equation of $h(PMMA) = -39.2 + 40.5c(PMMA)$ ($R^2 = 99.4$). This line does not pass through the origin, which indicates that there exists a substrate effect. However, this analysis is only for a rough calibration. The thickness in the final stack differs from these data since the PMMA penetrates the voids in the silica layers. The silica-layer was coated using the procedure described in section 2.3 on page 32.

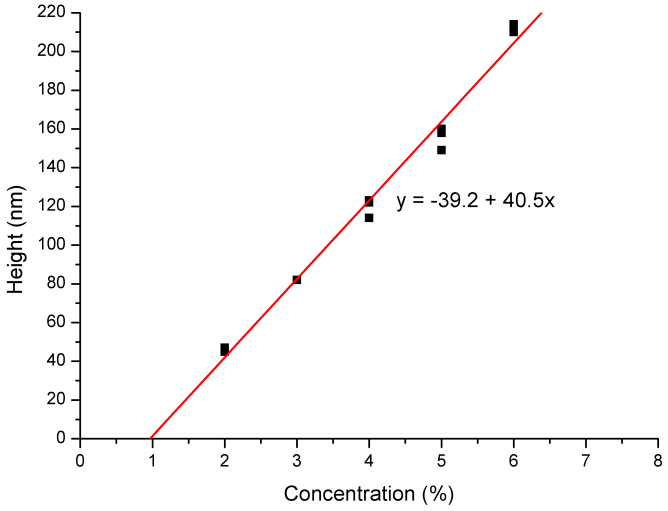

Figure 5-4.: Thickness of the spin-coated PMMA-layer vs. PMMA-concentration. The thickness was analyzed using a profilometer. The linear regression had a R^2 = 99.4 %.

The following concentrations were used:

Silica	34 g/l
PMMA	22 g/l

After each coating cycle, the samples were subjected to heat treatment at 100 °C for 15 min. The thicknesses of the individual layers were analyzed using cross-section SEM investigation (see Figure 5-5 on the next page). The individual layers displayed a constant thickness of 65 and 35 nm for silica and PMMA, respectively. Additionally, the theoretical calculations of the band structure with a shift in the thicknesses of ±5 nm indicate that the band structure was invariant to such variations.

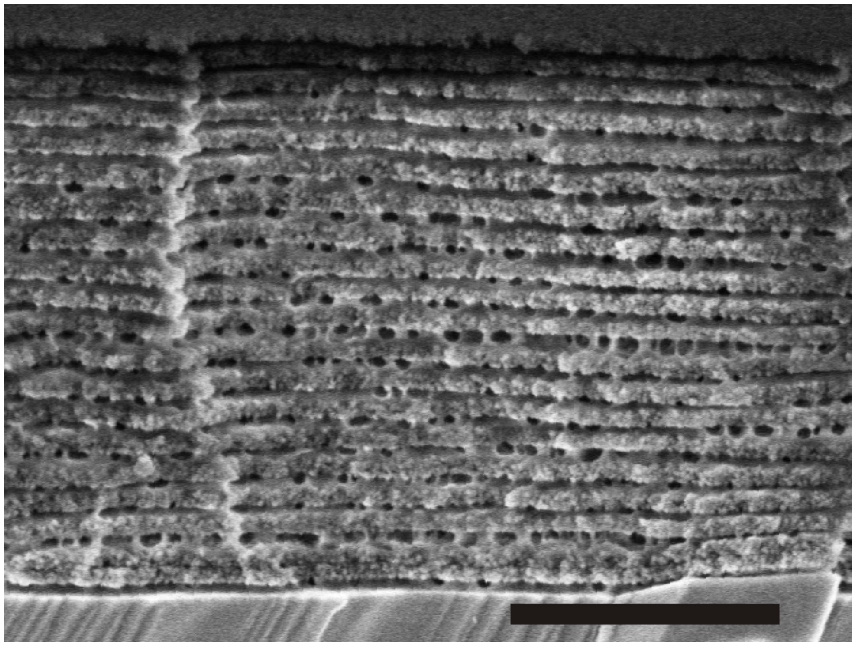

Figure 5-5.: Cross-section SEM image of the spincoated PMMA/SiO_2-stack. The scalebar equals 1 μm.

5.2.2. Characterization of the Sample via BLS

Parallel to the Surface

First the Brillouin spectra of the pure materials (nanocrystalline silica and PMMA) were compared to the 20-bilayer stack (compare for Figure 5-6 on the following page). The measurement was done in the transmission mode, so that $q_{\parallel}$ was analyzed. The spectra were collected at $q_{\parallel} = 0.0167\,nm^{-1}$ for in plane phonon propagation. Incident and scattered light were polarized in the plane of the film, i.e. perpendicular to the scattering plane.

The observed linear dependency $f(=\omega/2\pi)$ vs. q shows purely acoustic behavior for the phonon propagation in all samples. The longitudinal sound velocity corresponds to 2800 ± 30 and 3370 ± 30 m/s for PMMA and silica, respectively. The sound velocity of the porous silica is clearly lower than the velocity observed for normal glass (~5300 m/s). This is indicated by the solid line in Figure 5-6(b). This reduction in sound velocity can be attributed to the porosity of ca. 30 % of the nanocrystalline silica layer.

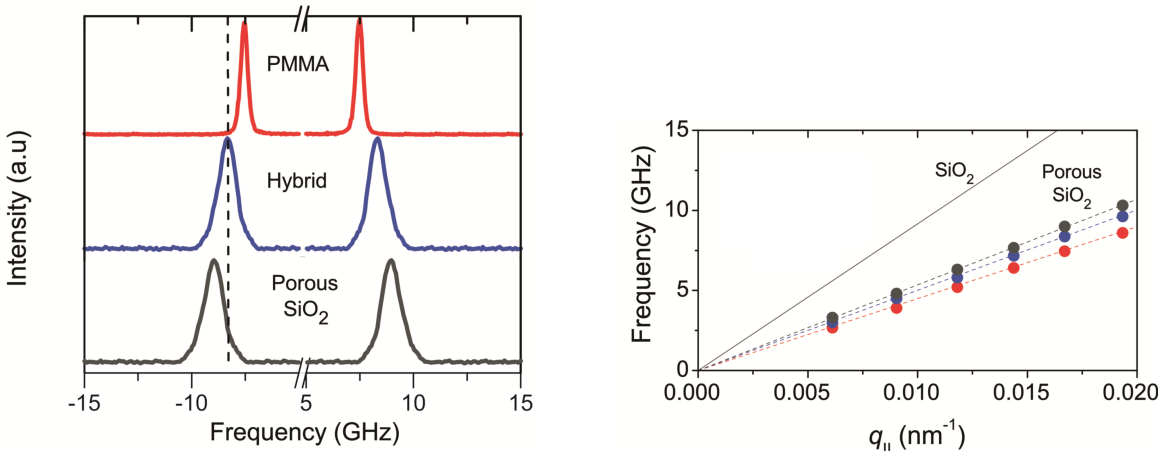

(a) BLS-spectra.

(b) Dispersion relation.

Figure 5-6.: a) Transmission BLS-spectra of a pure PMMA-film (top), a porous silica film (bottom) and the 20-BL stack (middle) at the same $q_{\parallel} = 0.0167\,nm^{-1}$. b) Dispersion relation for PMMA (red), porous silica (grey) and the stack (blue) for wave propagation parallel to the film. The dashed line shows the linear fit.

Since the probing length of the BLS setup is about $2\pi/q_{\parallel}$ (~380 nm) and each BL has a thickness of ~100 nm, the probing length exceeds the BL-thickness. Therefore, the obtained sound velocity, $c = \left(2\pi f/q_{\parallel}\right)$= 3160 m/s, falls in between the sound velocity of pure PMMA and the sound velocity of pure, nanoporous silica.

Assuming a homogeneous ($hq_{\parallel} \ll 1$, with h being the thickness) two component medium and the volume fraction of silica $\varnothing = 0.65$, the sound velocity c can be estimated using Wood's effective medium law:

$$\frac{1}{\rho c^2} = \frac{\varnothing}{\rho_{SiO_2} c_{SiO_2}^2} + \frac{1-\varnothing}{\rho_{PMMA} c_{PMMA}^2} \tag{5.3}$$

with $c_{PMMA} = 2800\,m/s$, $\rho_{PMMA} = 1.190\,g/cm^3$, $c_{SiO_2} = 3370\,m/s$ and $\rho_{SiO_2} = 1.42\,g/cm^3$. The computed value $c = 3150\,m/s$ is in excellent agreement with the experimental value (3160 $\pm$ 30 ms).

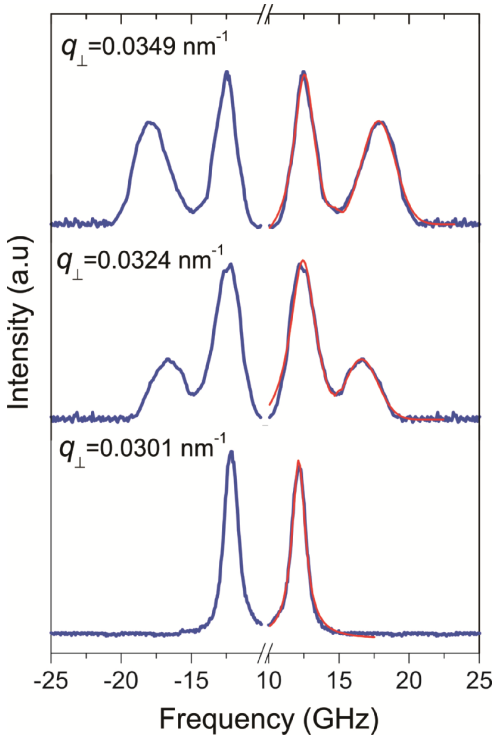

Figure 5-7.: Reflection BLS spectra of the hybrid SiO_2/PMMA film at three different $q_\perp$, near the Brillouin zone BZ boundary $q_{BZ} = 0.314\,nm^{-1}$. The data can be fittet with a single or double Lorentzian line shape (red line).

Perpendicular to the Surface

For phonon propagation perpendicular to the surface, a different behavior is observed. Figure 5-7 shows the polarized Brillouin spectra for three different scattering wave vectors near the Brillouin zone (BZ) boundary at $q_{BZ} \equiv G$ for the 1D stack; i.e. $q_{BZ}(= \pi/h) = 0.0314\,nm^{-1}$. For $q_\perp < q_{BZ}$ the BLS spectrum at $0.0301\,nm^{-1}$ displays one doublet. The spectrum then splits into two doublets when the value of $q_\perp$ crosses q_{BZ} as shown in the spectra at 0.0324 and $0.0349\,nm^{-1}$. This is direct evidence for the existence of a stop band in the phononic crystal due to their interference as a result of their discrete translational periodicity of the variable impedance structure along the film normal.

More information about the out-of-plane (along the uniaxial symmetry axis) phonon propa-

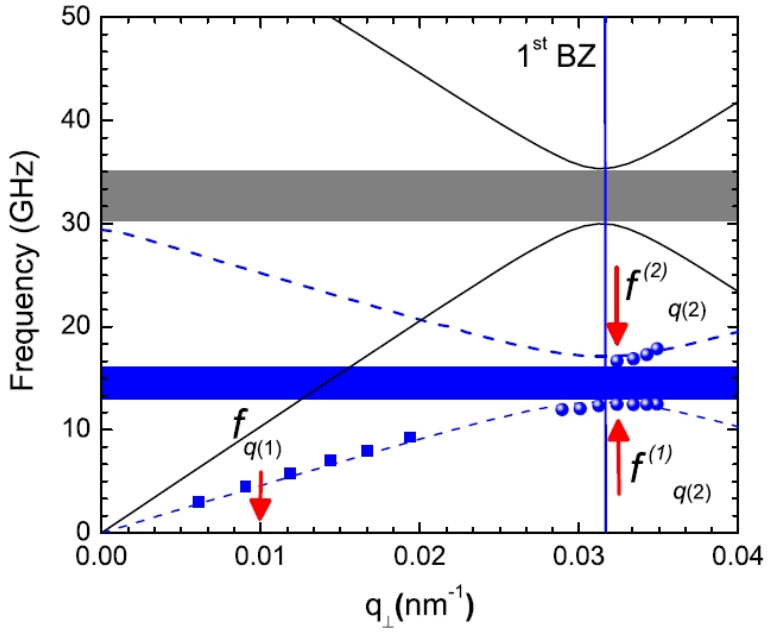

Figure 5-8.: Experimental dispersion relation for phonon propagation along the direction of periodicity. The highlighted blue region indicates the observed hypersonic band gap. The blue dashed and black solid lines correspond to the computed band diagram of PMMA/porous SiO_2 and PMMA/pure SiO_2, respectively. The solid circles and squares denote the experimental data for out-of-plane ($q_\perp$) and in-plane ($q_\parallel$, Figure 5-6(b) on page 68) propagation.

gation can obtained from the dispersion relation, $f^i(i=1,2)$ vs $q_\perp$. This is shown in Figure 5-8.

This dispersion relation reveals the presence of a stop band with a central frequency $f_g =$ 12.6 GHz and a width of $\Delta f_g = 4.5$ GHz, corresponding to a $\Delta f_g/f_g = 30$ %. This stop band opens at the first BZ (blue vertical line in Figure 5-8) and hence is a Bragg band.

The propagation of hypersonic longitudinal phonons in the direction normal to the layers for frequencies within the marked blue region is forbidden. Due to beam refraction in the reflection geometry[60], the low $q_\perp$ range is inaccessible. This missing acoustic branch (dashed blue line in Figure 5-8), however, is easily accessible for the in-plane phonon propagation (Figure 5-6(b)),

which is also shown in Figure 5-8 as solid squares.

The in-plane and the out-of-plane phonon propagation seems to fall into the same acoustic branch indicative of a single effective medium sound velocity along both directions for for long wavelength phonons.

Finite Element Analysis

In order to compute the phononic band structure, finite element analysis (FEA)[62, 63] was performed, solving the elastic wave equation in an infinite, 1D periodic medium. The model assumes perfectly bonded, ideally-flat, parallel layers with zero interfacial thickness and uniform respective layer thickness, no roughness or defects, with constant elastic properties within a given layer.

The porous silica layers were treated as an effective medium since experiments on a single silica layer (see Figure 5-6(b) on page 68) yielded effective medium behavior. The experimental values obtained from individual porous silica and PMMA layers were used directly in the calculation.

In general, interfaces exhibit some degree of roughness that might lead to incoherent scattering of higher frequency phonons and further suppression of phonon transport. However, the degree of this incoherent scattering component depends on the wavelength of the phonons probed in relation to the characteristic interface roughness; the interface roughness in the structure is typically < 30 nm, well below the effective medium requirement (~1/5 of probing wavelength).

Thus, the probed wavelengths are unable to resolve the inhomogeneities in the individual silica layer. Hence, we can model the system as an infinite one-dimensional periodic medium, with flat interfaces, for the frequency region of interest.

Figure 5-8 on the facing page visualizes the good agreement between the experimental and the theoretical dispersion relations. The dashed blue and solid black lines correspond to the

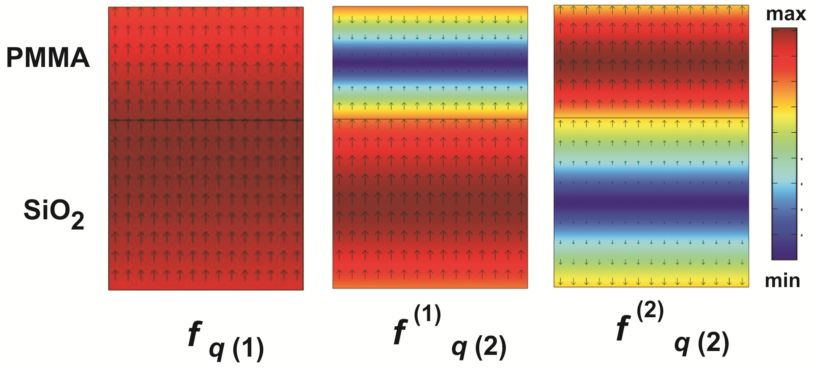

Figure 5-9.: Displacement field of lower band edge mode ($f^{(1)}$ at $q^{(2)}$) (middle), showing that the displacement fields are concentrated in the SiO_2 block and displacement field of upper band edge mode ($f^{(2)}$ at $q^{(2)}$) (right), showing that the displacement fields are concentrated in the PMMA block. The color bar shows displacement field variation. Left panel shows the displacement field for a low q value ($q^{(1)} = 0.01\,nm^{-1}$) where the system exhibits an effective medium behavior.

computed band diagram of PMMA/porous silica and PMMA/fused silica, respectively. For the latter system the Bragg gap has a center frequency of 30 GHz with a width of about 5 GHz ($\Delta f/f$ = 17 %) as indicated by the grey band, whereas for the PMMA/porous silica the gap mid frequency is at 15 GHz with a width of 4.5 GHz ($\Delta f/f$ = 30 %) as indicated by the blue band. The effect of porosity in the SiO_2 layer increases the center frequency, the width of the band gap remains roughly the same. This example shows the great influence of porosity onto the phononic band structure. The width of the gap is related to the impedance contrast of the component layers via the elastic constants (modulus, Poisson's ratio) as well as the mass densities.

The porous SiO_2 block retains a sizable band gap and, furthermore, lends itself as a possible structural scaffold for introducing subsequent secondary active media, such as optical dyes, to probe photon-phonon interactions[64–66] or as a route toward novel structures that combine periodicity with component layers having graded mechanical properties.

The computed displacement fields of the lower and upper band edge modes within a single repeat unit of a 100 nm bilayer are shown in Figure 5-9 on the preceding page. The displacement fields reflects the difference in nature of the modes. The lower modes are concentrated in the stiffer silica layers. The upper modes are concentrated in the softer PMMA layers. This is a consequence of the one-dimensional discrete translational periodicity of the phononic crystal that couples eigenmodes with k-vectors of $k = G/2$ and $-G/2$. These two modes interact and form the upper and lower band edge modes, opening a band gap in the process. As a result of the translational symmetry, the two band edge eigenmodes are stationary modes with the same period as the phononic crystal, but their displacement fields are phase shifted with respect to each other by half a period. This is a direct result of the symmetry coupling and is independent of the exact thicknesses of the PMMA and the silica layer; i.e. the lower (upper) edge mode will have the displacement field concentrated in the stiffer (softer) block, which is at lower (higher) energy. This distinction in the band edge modes is most clearly manifest in the one-dimensional periodic system. As expected for effective medium behavior, the displacement field is uniformly distributed in both layers for long wavelength phonon propagation.

5.3. Conclusion

This work demonstrates the excellent agreement between the theoretical band structure and the experimental results. It could be shown that the silica nanoparticles act as an effective medium. The porosity of the silica layer has great influence of the position of the band gap. This could be used to tune the phononic crystal by infiltration of the pores. A dye could be infiltrated into the pores to probe the photon-phonon interactions of the system.

The 1D phononic crystal is also an ideal case to prove the theoretical models since it is easier to model than a system with more dimensions.

5.4. Instrumentation of the BLS-Setup

Details about the setup can be found in the thesis of N. Gomopoulos[59].

A frequency-doubled Nd:YAG laser (coherence) with an output power of 100 mW and a wavelength of 532 nm was used. The laser was mounted onto the rotary arm of the goniometer (ALV). The laser beam is passed through a Glan polarizer, yielding a polarization (V) perpendicular to the scattering plane. The laser beam is then focused onto the sample ($\varnothing$ ~200 μm) in the center of the goniometer. The scattered light gets collected by an aperture and afterwards passes two conjugated lenses where in between a Glan analyzer is located. The light gets then focused into a Fabry-Perot interferometer (JRS Scientific Instruments). An avalanche photo diode (APD) serves as detector. The signal gets analyzed with an multi-channel-analyzer (MCA).

6. Summary

This work is focused on the development of high quality nanoporous 1D photonic crystals from spherical TiO_2 and SiO_2 nanoparticles – also known as Bragg stacks – and their applications in a surface emitting feedback laser, electrochromic Bragg stacks, and as acoustic band pass filters, i.e. a phononic crystal.

A key component for these applications is the ability to soak up molecular compounds, like sensitizing dyes or reactive species, in nanoscopic pores. The chosen approach is based on setting up nanoporous Bragg stacks from spherical nanoparticles. With a proposed pore size of 5 nm, the corresponding nanoparticles afford a typical diameter of approximately 20 to 25 nm. While a suitable SiO_2 nanoparticle product is obtainable, the corresponding for TiO_2 is not.

Therefore, in the ***first part*** of this work, a protocol for the synthesis of homodisperse TiO_2 nanoparticles was developed. The key step in the synthesis of these TiO_2 nanoparticles was the identification and application of 3,4-dihydroxyhydrocinnamic acid as a surfactant in the peptization of a Titanium(IV)-oxide-hydroxide precursor. The resulting TiO_2 nanoparticles (anatase) exhibit a spherical morphology and a sharp particle size distribution centered at 23 nm. In contrast to established protocols, this synthesis affords fewer steps and was highly reproducible.

In the ***second part***, a protocol for the production of high quality nanoporous Bragg stacks consisting of up to 12 bilayers of TiO_2 and SiO_2 nanoparticles with different single layer thicknesses was optimized. Afterwards each layer's thickness was calibrated on the basis of ellipsometric data so that they – and thus the energetic position of the stop band – were exclusively dependent on the concentration of the corresponding solutions of TiO_2 and SiO_2 nanoparticles

in a spin-coating process. Using this principle, 12-bilayer Bragg stacks with optical stop bands at 374, 486 and 686 nm and band widths of 89, 115 and 154 nm, respectively, were produced and characterized by means of UV-VIS spectroscopy and scanning electron microscopy.

In the ***third part***, a nanoporous Bragg stack optimized for lasing was manufactured from 12-bilayers, with each layer 106 nm thick, this lead to an optical stop band centered at 608 nm. After the Bragg stack was loaded with the established lasing dye Rhodamin 6G, the device displayed a stimulated emission near the blue edge of the stop band. The threshold energy density was 170 mJ/cm^2, and the system exhibited a Full width at half maximum of 6 nm.

In the ***fourth part***, different nanoporous Bragg stacks with stop bands centered at 400, 580 and 700 nm were manufactured on top of a WO_3 coated FTO glass. Upon an electric bias in a $LiClO_4$ / propylenecarbonate electrolyte, a reversible color change was observed due to the electrochromic effect of the WO_3 layer. The influence of the overall Bragg stack thickness on the kinetics of this color change was studied.

In the ***fifth part***, the concept of nanoporous Bragg stacks as 1D photonic crystals was transferred to phononic crystals. The original procedure was changed; an alternating spin-coating of SiO_2 nanoparticles and PMMA was used. The latter one was not introduced as a nanoparticle suspension but as pure solution. Thus, considerable amounts of the PMMA did not form isolated layers on top of the SiO_2 layers but filled the voids between the SiO_2 nanoparticles in the layers. Yet, a sufficiently strong contrast was achieved in the elastic moduli between the SiO_2 and the PMMA layers. According to Brillouin spectroscopic data the resulting 1D-phononic crystal exhibits a band gap with a central frequency $f_g = 12.6$ GHz and a width $\Delta f_g / f_g = 4.5$ GHz.

The results of this work have demonstrated the broad potential of high quality nanoporous Bragg stacks to a variety of applications.

A. Appendix

A.1. Pore Diameter

The pore diameter in nanoparticles that are arranged in a ccp lattice is equivalent to the maximal sphere size fitting into the tetrahedron gap[67]. The problem is sketched in Figure A-1.

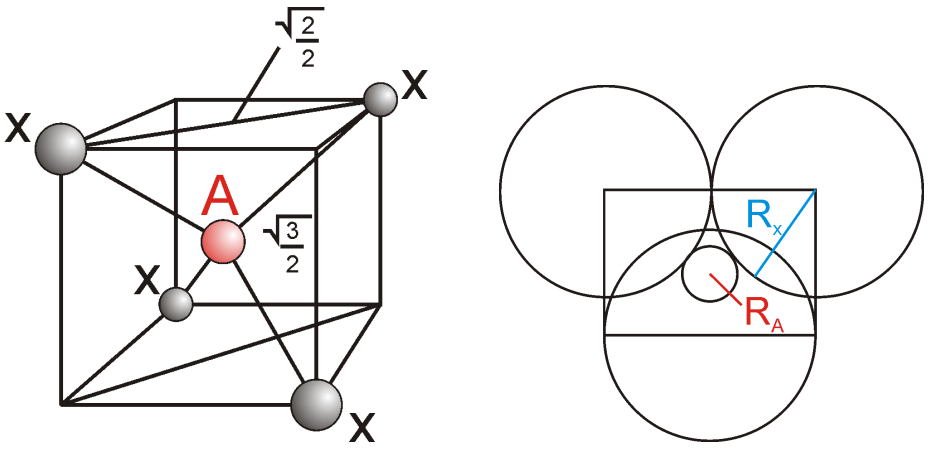

(a) Tetrahedron $A^{[4]}X_4$ inserted into a cube.

(b) Cut along (110) of a ccp.

Figure A-1.: Sketch of the tetrahedron gap.

It is $(R_A + R_X)/R_X = \sqrt{3}/\sqrt{2^3}$ and therefore:

$$\frac{R_A}{R_X} = \sqrt{\frac{3}{2}} - 1 = 0.225 \tag{A.1}$$

Assuming a pore diameter of 5 nm which is sufficient for a good dye loading, the particles need a minimum size of $R_A/0.225 = 5\ nm/0.225 = 22.22$ nm.

A.2. Surface Coverage of the Ligand

Assuming perfectly smooth spheres, the BET surface area per gram of nanomaterial can be estimated using simple algebra.

One gram of nanoparticles contains

$$n = \frac{6}{\pi d^3 \rho} \tag{A.2}$$

spheres with the diameter d and the density ρ. The particles have a surface area of

$$A = \text{number of particles} \cdot \text{surface area per particle} = \frac{6}{\pi d^3 \rho} \cdot \pi d^2 = \frac{6}{d\rho} \tag{A.3}$$

corrected for input of [nm] and yield of $[m^2/g]$

$$A(BET)[m^2/g] = \frac{6000}{d[nm]\rho[g/ml]} \tag{A.4}$$

This is only a very rough approximation, of course. However, assuming a particle diameter of 23 nm, a density of 3.9 g/l, an amount of 20.6 ml TIPO, the area per DHCA ligand of $9 \cdot 10^{-20}$ nm^2 and a molecular weight of DHCA of 182.17 g/mol, one gets an amount of 0.62 g of DHCA ligand, for 100 % surface coverage of the nanoparticles.

This value is not an exact match with the practically-used value (0.96 g), however, it is a close match, considering the many approximations that were used (roughness of the nanoparticles itself, adsorption/desorption processes, ...). It also makes sense that the particles have a larger surface area (more ligand is needed). This is attributed to surface roughness, a variable not considered in this calculation.

A.3. Ellipsometric Characterization

The results of the ellipsometric characterization are shown in Table A.1.

Table A.1.: Results from the ellipsometric characterization of the spin-coated samples.

	slope SiO_2	**R^2**	**slope TiO_2**	**R^2**
thickcal	1.46 nm/(g/l)	0.9975	0.90 nm/(g/l)	0.9988
multistack	97.8 nm/layer	0.9998	154 nm/layer	0.9995
stackcal	1.49 nm/(g/l)	0.9965	0.88 nm/(g/l)	0.9979

A.4. Appreviations

BZ	Brillouin Zone
DFB	Distributed Feedback
DHCA	3,4-Dihydroxyhydrocinnamic Acid
DOS	Density of States
FEA	Finite Element Analysis
FTO	Fluorine-Doped Tin Oxide
FWHM	Full Width at Half Maximum
ITO	Indium Tin Oxide
PC	Photonic Crystal
PL	Photoluminescence
PMMA	Poly(Methyl Methacrylate)
SDS	Sodium Dodecyl Sulfate
SEM	Scanning Electron Microscope
TCO	Transparent Conducting Oxide
TIPO	Titanium(IV) Isopropoxide
TMAOH	Tetramethylammonium Hydroxide
VASE	Various Angle Spectroscopic Ellipsometer

Bibliography

[1] J. D. Joannopoulos, R. D. Meade, and J. N. Winn, *Photonic Crystals: Molding the Flow of Light*. Princeton University Press, 2008.

[2] P. Vukusic and J. R. Sambles, "Photonic structures in biology," *Nature*, vol. 424, no. 6950, pp. 852–855, 2003.

[3] F. Fleischhaker and R. Zentel, "Opale: Photonische Kristalle," *Chemie in unserer Zeit*, vol. 41, no. 1, pp. 38–44, 2007.

[4] Wikipedia, "Morpho — wikipedia, the free encyclopedia," 2010. [Online; accessed 4-June-2010].

[5] Wikipedia, "Sea mouse — wikipedia, the free encyclopedia," 2010. [Online; accessed 4-June-2010].

[6] R. C. Schroden, M. Al-Daous, C. F. Blanford, and A. Stein, "Optical properties of inverse opal photonic crystals," *Chemistry of Materials*, vol. 14, no. 8, pp. 3305–3315, 2002.

[7] A. C. Arsenault, D. P. Puzzo, I. Manners, and G. A. Ozin, "Photonic-crystal full-colour displays," *Nat Photon*, vol. 1, no. 8, pp. 468–472, 2007.

[8] S. L. Kuai, G. Bader, and P. V. Ashrit, "Tunable electrochromic photonic crystals," *Applied Physics Letters*, vol. 86, no. 22, 2005.

[9] J. I. Chen, G. von Freymann, S. Y. Choi, V. Kitaev, and G. A. Ozin, "Amplified photochemistry with slow photons," *Advanced Materials*, vol. 18, no. 14, p. 1915, 2006.

[10] S. Colodrero, A. Mihi, J. A. Anta, M. Ocana, and H. Miguez, "Experimental Demonstration of the Mechanism of Light Harvesting Enhancement in Photonic-Crystal-Based Dye-Sensitized Solar Cells," *Journal of Physical Chemistry C*, vol. 113, no. 4, pp. 1150–1154, 2009.

[11] D. J. Norris and Y. A. Vlasov, "Chemical approaches to three-dimensional semiconductor photonic crystals," *Advanced Materials*, vol. 13, no. 6, pp. 371–376, 2001.

[12] A. Birner, R. B. Wehrspohn, U. M. Gosele, and K. Busch, "Silicon-based photonic crystals," *Advanced Materials*, vol. 13, pp. 377–388, MAR 16 2001.

[13] A. P. Li, F. Muller, A. Birner, K. Nielsch, and U. Gosele, "Hexagonal pore arrays with a 50–420 nm interpore distance formed by self-organization in anodic alumina," *Journal of Applied Physics*, vol. 84, no. 11, pp. 6023–6026, 1998.

[14] L. D. Bonifacio, B. V. Lotsch, D. P. Puzzo, F. Scotognella, and G. A. Ozin, "Stacking the Nanochemistry Deck: Structural and Compositional Diversity in One-Dimensional Photonic Crystals," *Advanced Materials*, vol. 21, no. 16, pp. 1641–1646, 2009.

[15] S. Y. Choi, M. Mamak, G. von Freymann, N. Chopra, and G. A. Ozin, "Mesoporous Bragg Stack Color Tunable Sensors," *Nano Letters*, vol. 6, no. 11, pp. 2456–2461, 2006.

[16] B. V. Lotsch and G. A. Ozin, "Clay Bragg Stack Optical Sensors," *Advanced Materials*, vol. 20, pp. 4079+, NOV 3 2008.

[17] J. Kobler, B. V. Lotsch, G. A. Ozin, and T. Bein, "Vapor-Sensitive Bragg Mirrors and Optical Isotherms from Mesoporous Nanoparticle Suspensions," *ACS Nano*, vol. 3, pp. 1669–1676, JUL 2009.

[18] S. D. Burnside, V. Shklover, C. Barbe, P. Comte, F. Arendse, K. Brooks, and M. Grätzel, "Self-Organization of TiO_2 Nanoparticles in Thin Films," *Chemistry of Materials*, vol. 10, no. 9, pp. 2419–2425, 1998.

[19] C. J. Barbé, F. Arendse, P. Comte, M. Jirousek, F. Lenzmann, V. Shklover, and M. Grätzel, "Nanocrystalline Titanium Oxide Electrodes for Photovoltaic Applications," *Journal of the American Ceramic Society*, vol. 80, no. 12, pp. 3157–3171, 1997.

[20] M. E. Calvo, O. Sànchez-Sobrado, S. Colodrero, and H. Míguez, "Control over the Structural and Optical Features of Nanoparticle-Based One-Dimensional Photonic Crystals," *Langmuir*, vol. 25, no. 4, pp. 2443–2448, 2009.

[21] C. V. Sterling and L. E. Scriven, "Interfacial turbulence: Hydrodynamic instability and the marangoni effect," *AICHE Journal*, vol. 5, no. 4, pp. 514–523, 1959.

[22] L. E. Scriven and C. V. Sterling, "Marangoni effects," *Nature*, vol. 187, no. 4733, pp. 186–188, 1960.

[23] M. E. Calvo, O. S. Sobrado, G. Lozano, and H. Míguez, "Molding with nanoparticle-based one-dimensional photonic crystals: A route to flexible and transferable Bragg mirrors of high dielectric contrast," *Journal of Materials Chemistry*, vol. 19, no. 20, pp. 3144–3148, 2009.

[24] S. Colodrero, A. Mihi, L. Haggman, M. Ocana, G. Boschloo, A. Hagfeldt, and H. Míguez, "Porous One-Dimensional Photonic Crystals Improve the Power-Conversion Efficiency of Dye-Sensitized Solar Cells," *Advanced Materials*, vol. 21, no. 7, p. 764, 2009.

[25] S. Colodrero, M. Ocana, A. R. Gonzalez-Elipe, and H. Míguez, "Response of nanoparticle-based one-dimensional photonic crystals to ambient vapor pressure," *Langmuir*, vol. 24, no. 16, pp. 9135–9139, 2008.

[26] S. Colodrero, M. Ocana, and H. Míguez, "Nanoparticle-based one-dimensional photonic crystals," *Langmuir*, vol. 24, no. 9, pp. 4430–4434, 2008.

[27] G. Lozano, S. Colodrero, O. Caulier, M. E. Calvo, and H. Míguez, "Theoretical Analysis of the Performance of One-Dimensional Photonic Crystal-Based Dye-Sensitized Solar Cells," *Journal of Physical Chemistry C*, vol. 114, no. 8, pp. 3681–3687, 2010.

[28] L. D. Bonifacio, D. P. Puzzo, S. Breslav, B. M. Willey, A. McGeer, and G. A. Ozin, "Towards the Photonic Nose: A Novel Platform for Molecule and Bacteria Identification," *Advanced Materials*, vol. 22, no. 12, p. 1351, 2010.

[29] P. G. O'Brien, D. P. Puzzo, A. Chutinan, L. D. Bonifacio, G. A. Ozin, and N. P. Kherani, "Selectively Transparent and Conducting Photonic Crystals," *Advanced Materials*, vol. 22, no. 5, p. 611, 2010.

[30] D. P. Puzzo, F. Scotognella, M. Zavelani-Rossi, M. Sebastian, A. J. Lough, I. Manners, G. Lanzani, R. Tubino, and G. A. Ozin, "Distributed Feedback Lasing from a Composite Poly(phenylene vinylene)-Nanoparticle One-Dimensional Photonic Crystal," *Nano Letters*, vol. 9, no. 12, pp. 4273–4278, 2009.

[31] J. . Pedersen, S. Xiao, and N. A. Mortensen, "Limits of slow light in photonic crystals," *Physical Review B*, vol. 78, no. 15, p. 153101, 2008.

[32] J. I. Chen, G. von Freymann, S. Y. Choi, V. Kitaev, and G. A. Ozin, "Slow photons in the fast lane in chemistry," *Journal of Materials Chemistry*, vol. 18, no. 4, pp. 369–373, 2008.

[33] J. I. Chen, G. von Freymann, V. Kitaev, and G. A. Ozin, "Effect of disorder on the optically amplified photocatalytic efficiency of titania inverse opals," *Journal of the American Chemical Society*, vol. 129, no. 5, pp. 1196–1202, 2007.

[34] J. I. L. Chen, E. Loso, N. Ebrahim, and G. A. Ozin, "Synergy of slow photon and chemi-

cally amplified photochemistry in platinum nanocluster-loaded inverse titania opals," *Journal of the American Chemical Society*, vol. 130, no. 16, p. 5420, 2008.

[35] J. I. Chen and G. A. Ozin, "Tracing the Effect of Slow Photons in Photoisomerization of Azobenzene," *Advanced Materials*, vol. 20, no. 24, p. 4784, 2008.

[36] A. Mihi and H. Míguez, "Origin of light-harvesting enhancement in colloidal-photonic-crystal-based dye-sensitized solar cells," *Journal of Physical Chemistry B*, vol. 109, no. 33, pp. 15968–15976, 2005.

[37] T. Komikado, S. Yoshida, and S. Umegaki, "Surface-emitting distributed-feedback dye laser of a polymeric multilayer fabricated by spin coating," *Applied Physics Letters*, vol. 89, no. 6, p. 061123, 2006.

[38] C. V. Shank, A. Dienes, and W. T. Silfvast, "Single pass gain of exciplex 4-MU and Rhodamin 6G Laser amplifiers," *Applied Physics Letters*, vol. 17, no. 7, pp. 307–309, 1970.

[39] M. Montalti, A., Credi, L., Prodi M., and T. Gandolfi, *Handbook of Photochemistry (3rd ed.)*. Taylor & Francis, Boca Raton FL, 2006.

[40] C. V. Shank, A. Dienes, and W. T. Silfvast, "SINGLE PASS GAIN OF EXCIPLEX 4-MU AND RHODAMINE 6G DYE LASER AMPLIFIERS," *Applied Physics Letters*, vol. 17, no. 7, pp. 307–309, 1970.

[41] M. N. Shkunov, Z. V. Vardeny, M. C. DeLong, R. C. Polson, A. A. Zakhidov, and R. H. Baughman, "Tunable, Gap-State Lasing in Switchable Directions for Opal Photonic Crystals," *Advanced Functional Materials*, vol. 12, no. 1, pp. 21–26, 2002.

[42] Y. Y. Li, F. Cunin, J. R. Link, T. Gao, R. E. Betts, S. H. Reiver, V. Chin, S. N. Bhatia, and M. J. Sailor, "Polymer Replicas of Photonic Porous Silicon for Sensing and Drug Delivery Applications," *Science*, vol. 299, no. 5615, pp. 2045–2047, 2003.

[43] L. Zhai, A. J. Nolte, R. E. Cohen, and M. F. Rubner, "pH-Gated Porosity Transitions of Polyelectrolyte Multilayers in Confined Geometries and Their Application as Tunable Bragg Reflectors," *Macromolecules*, vol. 37, no. 16, pp. 6113–6123, 2004.

[44] M. J. Sailor and J. Link, "'Smart dust': nanostructured devices in a grain of sand," *Chemical Communications*, no. 11, pp. 1375–1383, 2005.

[45] B. H. King, A. M. Ruminski, J. L. Snyder, and M. J. Sailor, "Optical-Fiber-Mounted Porous Silicon Photonic Crystals for Sensing Organic Vapor Breakthrough in Activated Carbon," *Advanced Materials*, vol. 19, no. 24, pp. 4530–4534, 2007.

[46] M. C. Fuertes, F. J. López-Alcaraz, M. C. Marchi, H. E. Troiani, V. Luca, H. Míguez, and G. J. A. A. Soler-Illia, "Photonic Crystals from Ordered Mesoporous Thin-Film Functional Building Blocks," *Advanced Functional Materials*, vol. 17, no. 8, pp. 1247–1254, 2007.

[47] Z. Wu, D. Lee, M. F. Rubner, and R. E. Cohen, "Structural Color in Porous, Superhydrophilic, and Self-Cleaning SiO_2 Bragg Stacks," *Small*, vol. 3, no. 8, pp. 1445–1451, 2007.

[48] D. Lee, D. Omolade, R. E. Cohen, and M. F. Rubner, "pH-Dependent Structure and Properties of TiO_2/SiO_2 Nanoparticle Multilayer Thin Films," *Chemistry of Materials*, vol. 19, no. 6, pp. 1427–1433, 2007.

[49] D. R. Rosseinsky and R. J. Mortimer, "Electrochromic systems and the prospects for devices," *Advanced Materials*, vol. 13, no. 11, pp. 783–+, 2001.

[50] N. I. Jaksic and C. Salahifar, "A feasibility study of electrochromic windows in vehicles," *Solar Energy Materials and Solar Cells*, vol. 79, no. 4, pp. 409–423, 2003.

[51] C. G. Granqvist, "Electrochromic tungsten oxide films: Review of progress 1993-1998," *Solar Energy Materials and Solar Cells*, vol. 60, no. 3, pp. 201 – 262, 2000.

[52] N. Ozer and C. M. Lampert, "Electrochromic performance of sol-gel deposited WO_3-V_2O_5 films," *Thin Solid Films*, vol. 349, no. 1-2, pp. 205 – 211, 1999.

[53] M.-A. De Paoli, A. Zanelli, M. Mastragostino, and A. M. Rocco, "An electrochromic device combining polypyrrole and WO_3 II: solid-state device with polymeric electrolyte," *Journal of Electroanalytical Chemistry*, vol. 435, no. 1-2, pp. 217 – 224, 1997.

[54] O. Pyper, A. Kaschner, and c. Thomsen, "In situ Raman spectroscopy of the electrochemical reduction of WO_3 thin films in various electrolytes," *Solar Energy Materials and Solar Cells*, vol. 71, no. 4, pp. 511 – 522, 2002.

[55] Q. Zhong, J. R. Dahn, and K. Colbow, "Lithium intercalation into WO_3 and the phase diagram of Li_xWO_3," *Physical Review B*, vol. 46, pp. 2554–2560, Jul 1992.

[56] N. Sharma, M. Deepa, P. Varshney, and S. A. Agnihotry, "Influence of organic additive on the morphological, electrical and electrochromic properties of sol-gel derived WO_3 coatings," *Journal of Sol-Gel Science and Technology*, vol. 18, no. 2, pp. 167–173, 2000.

[57] T. Kudo, H. Okamoto, K. Matsumoto, and Y. Sasaki, "Peroxopolytungstic acids synthesized by direct reaction of tungsten or tungsten carbide with hydrogen peroxide," *Inorganica Chimica Acta*, vol. 111, no. 2, pp. L27 – L28, 1986.

[58] A. Bessiere, J. C. Badot, M. C. Certiat, J. Livage, V. Lucas, and N. Baffier, "Sol-gel deposition of electrochromic WO_3 thin film on flexible ITO/PET substrate," *Electrochimica Acta*, vol. 46, no. 13-14, pp. 2251–2256, 2001.

[59] N. Gomopoulos, *Nanomechanical and Phononic Properties of Structured Soft Materials*. PhD thesis, Johannes Gutenberg–Universität Mainz, 2009.

[60] N. Gomopoulos, W. Cheng, M. Efremov, P. F. Nealey, and G. Fytas, "Out-of-Plane Longitudinal Elastic Modulus of Supported Polymer Thin Films," *Macromolecules*, vol. 42, no. 18, pp. 7164–7167, 2009.

[61] N. W. Ashcroft and N. D. Mermin, *Solid State Physics*. Saunders College Publishing, 1976.

[62] T. Gorishnyy, C. K. Ullal, M. Maldovan, G. Fytas, and E. L. Thomas, "Hypersonic Phononic Crystals," *Physical Review Letters*, vol. 94, p. 115501, Mar 2005.

[63] J.-H. Jang, C. K. Ullal, T. Gorishnyy, V. V. Tsukruk, and E. L. Thomas, "Mechanically Tunable Three-Dimensional Elastomeric Network/Air Structures via Interference Lithography," *Nano Letters*, vol. 6, no. 4, pp. 740–743, 2006.

[64] J. Yoon, W. Lee, J.-M. Caruge, M. Bawendi, E. L. Thomas, S. Kooi, and P. Prasad, "Defect-mode mirrorless lasing in dye-doped organic/inorganic hybrid one-dimensional photonic crystal," *Applied Physics Letters*, vol. 88, no. 9, p. 091102, 2006.

[65] M. Maldovan and E. L. Thomas, "Simultaneous localization of photons and phonons in two-dimensional periodic structures," *Applied Physics Letters*, vol. 88, no. 25, p. 251907, 2006.

[66] M. Eichenfield, J. Chan, R. M. Camacho, K. J. Vahala, and O. Painter, "Optomechanical crystals," *Nature*, vol. 462, no. 7269, pp. 78–82, 2009.

[67] W. Borchardt-Ott, *Kristallographie: Eine Einführung für Naturwissenschaftler*. Springer, Berlin, 2010.

Index